



1 **Contribution of expanded marine sulfur chemistry to the seasonal variability**
2 **of DMS oxidation products and size-resolved sulfate aerosol**

3 Linia Tashmim¹, William C. Porter¹, Qianjie Chen², Becky Alexander³, Charles H. Fite⁴,
4 Christopher D. Holmes⁴, Jeffrey R. Pierce⁵, Betty Croft⁶, and Sakiko Ishino⁷

5 ¹Department of Environmental Sciences, University of California, Riverside, CA, USA

6 ²Department of Civil and Environmental Engineering, The Hong Kong Polytechnic University,
7 Hong Kong, China

8 ³Department of Atmospheric Sciences, University of Washington, Seattle, WA, USA

9 ⁴Department of Earth, Ocean and Atmospheric Science, Florida State University, Tallahassee,
10 FL, USA

11 ⁵Department of Atmospheric Science, Colorado State University, Fort Collins, CO, USA

12 ⁶Department of Physics and Atmospheric Science, Dalhousie University, Halifax, Nova Scotia,
13 Canada

14 ⁷Institute of Nature and Environmental Technology, Kanazawa University, Japan

15 Correspondence: Linia Tashmim (ltash001@ucr.edu) and William C. Porter
16 (william.porter@ucr.edu)

17 **Abstract.** Marine emissions of dimethyl sulfide (DMS) and the subsequent formation of its
18 oxidation products methane sulfonic acid (MSA) and sulfuric acid (H₂SO₄) are well-known natural
19 precursors of atmospheric aerosols, contributing to particle mass and cloud formation over ocean
20 and coastal regions. Despite a long-recognized and well-studied role in the marine troposphere,
21 DMS oxidation chemistry remains a work in progress within many current air quality and climate
22 models, with recent advances exploring heterogeneous chemistry and uncovering previously
23 unknown intermediate species. With the identification of additional DMS oxidation pathways and
24 intermediate species influencing its eventual fate, it is important to understand the impact of these
25 pathways on the overall sulfate aerosol budget and aerosol size distribution. In this work, we
26 update and evaluate the DMS oxidation mechanism of the chemical transport model GEOS-Chem
27 by implementing expanded DMS oxidation pathways into the model. These updates include gas-
28 and aqueous-phase reactions, the formation of the intermediates dimethyl sulfoxide (DMSO) and
29 methane sulphinic acid (MSIA), as well as cloud loss and aerosol uptake of the recently quantified
30 intermediate hydroperoxymethyl thioformate (HPMTF). We find that this updated mechanism
31 collectively decreases the global mean surface-layer gas-phase sulfur dioxide (SO₂) mixing ratio
32 by 38% and enhances sulfate aerosol (SO₄²⁻) mixing ratio by 16%. We further perform sensitivity
33 analyses exploring the contribution of cloud loss and aerosol uptake of HPMTF to the overall
34 sulfur budget. Comparing modeled concentrations to available observations we find improved
35 biases relative to previous studies. To quantify impacts of these chemistry updates on global
36 particle size distributions and mass concentration we use the TOMAS aerosol microphysics
37 module, finding changes in particle formation and growth affect the size distribution of aerosol.
38 With this new DMS-oxidation scheme the global annual mean surface layer number concentration
39 of particles with diameters smaller than 80 nm decreases by 12%, with cloud loss processes related
40 to HPMTF mostly responsible for this reduction. However, global annual mean number of particles
41 larger than 80 nm increases by 4.5%, suggesting that the new scheme promotes seasonal particle
42 growth to these sizes capable of acting as cloud condensation nuclei (CCN).



43 1 Introduction

44 Dimethyl sulfide (DMS: CH_3SCH_3) is the most abundant biological source of sulfate aerosol and
45 has a significant influence on Earth's radiation budget and climate due to its contribution to
46 atmospheric marine particle (Charlson et al., 1987; Fung et al., 2022). In the atmosphere, DMS
47 reacts with hydroxyl radical (OH), nitrate radical (NO_3), ozone (O_3) and various halogen species
48 (e.g., chlorine [Cl] and bromine oxide [BrO]), primarily forming sulfur dioxide (SO_2) and methyl
49 sulfonic acid (MSA; $\text{CH}_3\text{SO}_3\text{H}$) (Chen et al., 2018; Faloon, 2009; Hoffmann et al., 2016). These
50 oxidation products are considered key influences on the formation and evolution of natural
51 aerosols and clouds along with their associated climate impacts, especially in the marine boundary
52 layer (MBL) (Carslaw et al., 2013; Sipilä et al., 2010; Schobesberger et al., 2013; Thomas et al.,
53 2010; von Glasow and Crutzen, 2004). SO_2 and MSA formed by DMS oxidation can be deposited
54 on Earth surface or further oxidize affecting the size distribution of aerosol and cloud microphysics
55 (Leaitch et al., 2013; Wollesen de Jonge et al., 2021). SO_2 can either oxidize in the gas-phase by
56 reaction with the OH radical forming H_2SO_4 , which can participate in nucleation and early growth
57 of particles in the atmosphere, or it can be taken up by cloud droplets and undergo aqueous phase
58 oxidation by reaction with H_2O_2 or O_3 , forming SO_4^{2-} and generally only contributing to the growth
59 of aerosol particles (Hoyle et al., 2016; Kulmala, 2003). The hypohalous acids (HOBr, HOCl,
60 HOI) also plays significant role in aqueous-phase sulfate production in the marine boundary layer
61 (MBL) (Chen et al., 2016; Sherwen et al., 2016b). Recent studies have highlighted the importance
62 of natural aerosols originating from DMS oxidation and their contribution to the uncertainty of
63 aerosol radiative forcing in climate models (Carslaw et al., 2013; Fung et al., 2022; Rosati et al.,
64 2022; Novak et al., 2021, 2022). Since DMS-derived aerosol is a major source of uncertainty in
65 estimating the global natural aerosol burden and associated aerosol indirect radiative forcing, a
66 more accurate representation of DMS oxidation and particle formation processes is an important
67 step towards improved Earth system and climate modeling.

68 Although the chemistry of DMS oxidation has been previously studied in great detail, known
69 uncertainties and omissions in the current mechanism remain in current air quality and chemical
70 transport models (Barnes et al., 2006; Fung et al., 2022; Hoffmann et al., 2016, 2021). Furthermore,
71 while increasingly complex and experimentally validated mechanisms are under ongoing
72 development, DMS oxidation processes in many current chemical transport models continue to be
73 represented through simplified gas-phase reactions with the tropospheric oxidants OH and NO_3 ,
74 producing the two major oxidation products SO_2 and MSA at a fixed ratio as shown in R1-R3 in
75 Table 1 (Chen et al., 2018; Chin et al., 1996; Veres et al., 2020). This type of simplified mechanism
76 neglects the formation and loss of important intermediates such as dimethyl sulfoxide (DMSO:
77 CH_3SOCH_3), methane sulphinic acid (MSIA: $\text{CH}_3\text{SO}_2\text{H}$) and the recently discovered oxidation
78 product hydroperoxymethyl thioformate (HPMTF: $\text{HOOCH}_2\text{SCHO}$) (Berndt et al., 2019; Veres et
79 al., 2020; Wu et al., 2015).

80 These omissions can have major consequences on product yields of DMS oxidation, thereby
81 affecting the aerosol burdens. For example, the multiphase OH-addition pathway has been
82 identified as a dominant source of MSA, some of which subsequently undergoes aqueous-phase
83 oxidation to form sulfate aerosol (Chen et al., 2018; Ishino et al., 2021; Zhu et al., 2006; von
84 Glasow and Crutzen, 2004). Previous studies suggest that BrO contributes to 8 – 30% of total DMS
85 loss, highlighting the importance of this pathway as well (Breider et al., 2010; Boucher et al., 2003;
86 Chen et al., 2018; Khan et al., 2016). More recent experimental and laboratory studies have



87 confirmed the formation of methylthiomethylperoxy radicals (MSP; $\text{CH}_3\text{CH}_2\text{OO}$) from the H-
88 abstraction channel of OH oxidation, which can subsequently lead to a series of rapid
89 intramolecular H-shift isomerization reactions, ultimately resulting in the formation of the stable
90 intermediate HPMTF for 30–50% of annual total DMS oxidation (Berndt et al., 2019; Veres et al.,
91 2020; Vermeuel et al., 2020; Wu et al., 2015). Subsequent investigation of the isomerization rate
92 and heterogeneous loss of HPMTF in cloud droplets and aerosol shows a high production rate of
93 marine carbonyl sulfide from the chemical loss of HPMTF, a potential precursor of stratospheric
94 sulfate aerosol and significant inhibitor of cloud condensation nuclei (CCN) formation due to the
95 resulting reduction of surface SO_2 (Jernigan et al., 2022a).
96

97 **Table 1.** The three DMS oxidation reactions in the standard GEOS-Chem chemical mechanism

$\text{DMS} + \text{OH}_{(\text{abstraction})} \rightarrow \text{SO}_2 + \text{CH}_3\text{O}_2 + \text{CH}_2\text{O}$	(R1)
$\text{DMS} + \text{OH}_{(\text{addition})} \rightarrow 0.75 \text{SO}_2 + 0.25 \text{MSA} + \text{CH}_3\text{O}_2$	(R2)
$\text{DMS} + \text{NO}_3 \rightarrow \text{SO}_2 + \text{HNO}_3 + \text{CH}_3\text{O}_2 + \text{CH}_2\text{O}$	(R3)

98
99 Considering these and other consequences of complex DMS oxidation processes, a heavily
100 simplified oxidation scheme will necessarily neglect potentially important reaction intermediates
101 along with their production and loss pathways, with implications for the concentration and
102 distribution of the oxidation products, including particulate sulfate. Differing intermediate
103 lifetimes further influence sulfur removal and transport depending on the relative dominance of
104 pathways. Thus, the exclusion of key pathways and intermediate species can lead to errors in the
105 representation of the spatial distribution of both gas- and particle-phase sulfur species, as well as
106 global sulfur burden.

107 The DMS oxidation products sulfate and MSA play an important role in Earth's radiative budget
108 through cloud droplet formation, and the extent of this role depends on how efficiently they can
109 produce and grow new particles in the marine atmosphere (Thomas et al., 2010). SO_2 can oxidize
110 in the gas-phase the forming H_2SO_4 , which acts as a key product contributing to nucleation and
111 condensational growth as shown in Figure 1. SO_2 oxidizing through aqueous chemistry in cloud
112 droplets does contribute to particle growth rates by providing larger aerosol during cloud
113 evaporation that acts as more efficient CCN (Kaufman and Tanré, 1994). On the other hand, MSA
114 might participates in nucleation along with sulfuric acid in presence of amines or ammonia
115 (Johnson and Jen, 2023). Recent studies have highlighted the importance of aqueous-phase
116 chemistry in the formation and loss of MSA (Boniface et al., 2000; Chen et al., 2015; Kaufman
117 and Tanré, 1994; Kulmala et al., 2000).

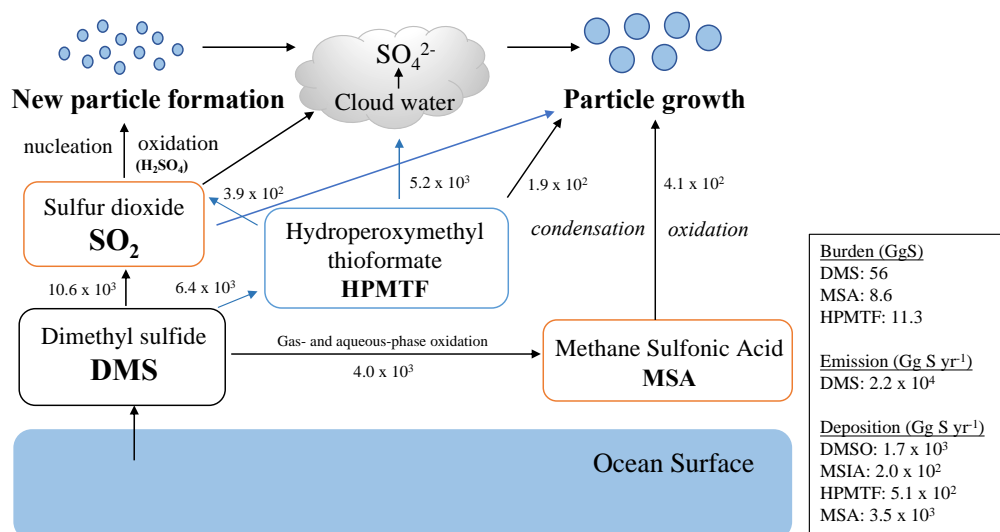


Figure 1 DMS oxidation mechanism used in this work showing formation of major stable oxidation products (green boxes) including newly identified intermediate HPMTF (blue box) and their contribution to new particle formation or growth of existing particles. Production and loss rate on arrows are in units of Gg S yr⁻¹.

118 Additionally, the recently identified intermediate HPMTF also has the potential for further gas-
 119 phase oxidation. Under cloud-free conditions, HPMTF can undergo gas-phase oxidation by OH,
 120 producing SO_2 and eventually leading to the formation of non-sea-salt- SO_4^{2-} . This sulfate can
 121 contribute to aerosol formation and growth processes, with climate implications (Galí et al., 2019).
 122 Other work has used direct airborne eddy covariance flux measurements to explain the chemical
 123 fate of HPMTF in the MBL finding that in cloudy conditions chemical loss due to aqueous phase
 124 reactions in cloud is the major HPMTF removal process, resulting in a 35% reduction in global
 125 SO_2 production from DMS and a 24% reduction in the near-surface SO_2 concentrations (0 to 3
 126 km) over the ocean (Novak et al., 2021). Thus, a complete representation of cloud loss and aerosol
 127 uptake is needed to effectively evaluate the atmospheric impacts of marine DMS and their
 128 connections to cloud formation (Novak et al., 2021; Holmes et al., 2019).

129 To better understand the marine sulfur budget, as well as the eventual formation, size distribution,
 130 and seasonality of sulfate aerosol, we use the global chemical transport model GEOS-Chem,
 131 integrating previously developed mechanisms along with newly proposed pathways involving the
 132 formation and loss of the intermediates DMSO, MSIA, and HPMTF. As part of this work, we
 133 further quantify the atmospheric impacts of individual reactions and mechanisms, evaluate
 134 uncertainties in the chemical mechanism, and identify improvements necessary to better represent
 135 the impacts of DMS more accurately on atmospheric chemistry and climate. The resulting
 136 integrated scheme provides a more complete representation of marine sulfur and sulfate aerosol
 137 species in marine tropospheric environments compared to the simplified base GEOS-Chem
 138 mechanism, with improved comparisons to aircraft and surface observations. Since aerosols are a
 139 major contributor to uncertainty in climate forcing, improving oxidation and aerosol formation
 140 mechanisms by adding and optimizing neglected reactions in models is a crucial step towards a
 141 more mechanistically robust representation of particle yields and sensitivities. We further perform
 142 multiple sensitivity tests to investigate how the uncertainty in heterogeneous uptake of the newly



143 identified HPMTF could influence DMS chemistry and tropospheric aerosol formation (Holmes
144 et al., 2019; Novak et al., 2021). In a broader sense our work provides a more detailed story on the
145 heterogeneous loss, fate, and ultimate impacts of DMS and its oxidation products, improving our
146 understanding of a key ocean-atmosphere interaction in the context of global change.



147 2 Methodology

148 To investigate modeled impacts on simulated aerosol size, number and mass concentration, aerosol
149 microphysics simulations are performed with Two-Moment Aerosol Sectional (TOMAS)
150 microphysics module available in GEOS-Chem v12.9.3 (GC-TOMAS)
151 (<https://github.com/geoschem/geos-chem/tree/12.9.3>) (Adams and Seinfeld, 2002; Kodros and
152 Pierce, 2017). In this study, TOMAS tracks aerosol number and the mass of each aerosol species
153 in 15 logarithmically sized bins, with sizes in this analysis ranging from 3 nm to 10 μm (Lee and
154 Adams, 2012; Lee et al., 2013). All binned aerosol species undergo interactive microphysics,
155 allowing the calculation of aerosol number budgets (Westervelt et al., 2013). The version of GC-
156 TOMAS used here includes 47 vertical levels, a horizontal resolution of $4^\circ \times 5^\circ$, and the GEOS-
157 FP data product for meteorological inputs. Simulations are performed for 2018, with 11 months of
158 discarded model spin up. Nucleation is simulated via a ternary nucleation scheme involving water,
159 sulfuric acid, and ammonia with nucleation rates scaled by 10^{-5} (Napari et al., 2002; Westervelt et
160 al., 2013). In low-ammonia regions (less than 1 pptv), a binary nucleation scheme involving water
161 and sulfuric acid is instead used (Vehkamäki et al., 2002). Previously GC-TOMAS has been used
162 for aerosol simulations to investigate topics such as the aerosol cloud-albedo effect and cloud
163 condensation nuclei formation (Kodros et al., 2016; Kodros and Pierce, 2017; Pierce and Adams,
164 2006; Westervelt et al., 2013). Aerosol species available for GC-TOMAS simulations are sulfate,
165 aerosol water, black carbon, organic carbon, mineral dust, and sea salt (Alexander et al., 2005;
166 Bey et al., 2001; Duncan Fairlie et al., 2007; Pye et al., 2009). The wet and dry deposition scheme
167 for aerosols and gas species are based on previous studies (Amos et al., 2012; Emerson et al., 2020;
168 Liu et al., 2001; Wesely, 1989; Wang et al., 1998).

169 The default GEOS-Chem chemical mechanism contains detailed HO_x – NO_x – VOC – O_3 –halogen
170 tropospheric chemistry along with recently updated halogen chemistry and in-cloud processing
171 (Bey et al., 2001; Holmes et al., 2019; Chen et al., 2017; Parrella et al., 2012; Schmidt et al., 2016;
172 Wang et al., 2019). The DMS emission flux from ocean are controlled by a gas transfer velocity
173 which is dependent on sea surface temperature and wind speed and a climatology of concentrations
174 in seawater (Johnson, 2010; Lana et al., 2011; Nightingale et al., 2000). The aqueous-phase
175 concentration of O_3 in aerosols or cloud droplets is calculated assuming gas-liquid equilibrium and
176 aqueous-phase concentration of OH is calculated following $[\text{OH}_{(\text{aq})}] = \delta[\text{OH}_{(\text{g})}]$ where, $\delta = 1 \times 10^{-19}$
177 $\text{M cm}^3 \text{ molecule}^{-1}$ (Jacob et al., 2005; Chen et al., 2018).

178 We refer to simulations performed using only these three DMS oxidation reactions (Table 1) as
179 the “BASE”, involving only the direct formation of SO_2 and MSA in gas-phase (Chin et al., 1996).
180 We further implement and evaluate a custom chemical mechanism for DMS oxidation, referred to
181 as “MOD” (Table 2-4), representing an integration of three individual DMS oxidation mechanism
182 updates explored previously using GEOS-Chem and CAM6-Chem, along with HPMTF loss via
183 heterogeneous chemistry in clouds and aerosols and dry and wet deposition of HPMTF (Chen et
184 al., 2018; Fung et al., 2022; Veres et al., 2020; Novak et al., 2021). Loss of HPMTF in clouds
185 follow entrainment-limited uptake which used a chemical rate expression to control rate of mixing
186 between cloudy and clear air (Holmes et al., 2019). In GC-TOMAS we use specific subroutine that
187 take amount of sulfate produced via in-cloud oxidation and condense it into an existing aerosol
188 size distribution. So, mass of sulfate produced by oxidation is portioned to the various size bins
189 according to the number of particles in that size bin. TOMAS microphysics accounts for H_2SO_4
190 formation based on gas-phase oxidation of SO_2 included in the kinetic preprocessor (KPP)



191 equation list valid for the simulation BASE. Since there are additional sources of sulfate in the
 192 integrated DMS oxidation mechanism both in gas and aqueous phase, we made necessary changes
 193 in the KPP code to explicitly track H₂SO₄ formation by gas phase oxidation of SO₂. On the other
 194 hand, code changes for sulfate formed by heterogeneous oxidation of MSA and HPMTF (in clouds
 195 and aerosols) were added in the GEOS-Chem microphysics module that also handles in-cloud
 196 oxidation of SO₂ in GC version 12.9.3 (Park et al., 2004; Trivitayanurak et al., 2008).

197 **Table 2.** Overview of the DMS oxidation mechanism via OH-addition pathway (Chen et al., 2018).

Gas-phase reactions	Rate (s ⁻¹)	References
DMS + OH → 0.60SO ₂ + 0.4MSA + CH ₃ O ₂	$8.2 \times 10^{-39} [\text{O}_2] e^{5376/T} / (1 + 1.05 \times 10^{-5} ([\text{O}_2]/[\text{M}]) e^{3644/T}) \text{ cm}^3 \text{ molecule}^{-1} \text{ s}^{-1}$	(Burkholder et al., 2015; Pham et al., 1995; Spracklen et al., 2005)
DMS + NO ₃ → SO ₂ + HNO ₃ + CH ₃ O ₂ + CH ₂ O	$1.90 \times 10^{-13} \exp(530/T)$	(Burkholder et al., 2015)
DMS + BrO → DMSO + Br	$1.40 \times 10^{-14} \exp(950/T)$	(Burkholder et al., 2015)
DMS + O ₃ → SO ₂	1.00e-19	(Burkholder et al., 2015; Du et al., 2007)
DMS + Cl → 0.5SO ₂ + 0.5DMSO + 0.5HCl + 0.5ClO	3.40e-10	(Barnes et al., 2006; Burkholder et al., 2015)
DMSO + OH → 0.95MSIA + 0.05SO ₂	$6.10 \times 10^{-12} \exp(800/T)$	(Burkholder et al., 2015; von Glasow and Crutzen, 2004)
MSIA + OH → 0.9SO ₂ + 0.1MSA	9.00e-11	(Burkholder et al., 2015)
MSIA + O ₃ → MSA	2.00e-18	(von Glasow and Crutzen, 2004; Lucas and Prinn, 2002)

198

Aqueous-phase reactions	k ₂₉₈ [M ⁻¹ s ⁻¹]	References
DMS (aq) + O ₃ (aq) → DMSO (aq) + O ₂ (aq)	8.61×10^8	(Gershenson et al., 2001)
DMSO (aq) + OH (aq) → MSIA (aq)	6.63×10^9	(Zhu et al., 2003)
MSIA (aq) + OH (aq) → MSA (aq)	6.00×10^9	(Sehested and Holcman, 1996)
MSI ⁻ (aq) + OH (aq) → MSA (aq)	1.20×10^{10}	(Bardouki et al., 2002)
MSIA (aq) + O ₃ (aq) → MSA (aq)	3.50×10^7	(Hoffmann et al., 2016)
MSI ⁻ (aq) + O ₃ (aq) → MSA (aq)	2.00×10^6	(Flyunt et al., 2001)
MSA (aq) + OH (aq) → SO ₄ ²⁻	1.50×10^7	(Hoffmann et al., 2016)
MS ⁻ (aq) + OH (aq) → SO ₄ ²⁻ (aq)	1.29×10^7	(Zhu et al., 2003)

199

200

Table 3. Overview of the DMS oxidation mechanism involving HPMTF formation (Veres et al., 2020).

Gas-phase reactions	Rate (s ⁻¹)	Original References
MSP → OOCCH ₂ SCH ₂ OOH	$2.2433 \times 10^{11} \exp(-9.8016 \times 10^3/T) * (1.0348 \times 10^8/T^3)$	(Berndt et al., 2019; Veres et al., 2020; Wollesen de Jonge et al., 2021)
OOCCH ₂ SCH ₂ OOH → HPMTF (HOOCH ₂ SCHO) + OH	$6.0970 \times 10^{11} \exp(-9.489 \times 10^3/T) * (1.1028 \times 10^8/T^3)$	(Berndt et al., 2019; Veres et al., 2020; Wollesen de Jonge et al., 2021)
OOCCH ₂ SCH ₂ OOH + NO → HOOCH ₂ SCH ₂ O + NO ₂	$4.9 \times 10^{-12} \exp(260/T)$	(Saunders et al., 2003)
HOOCH ₂ SCH ₂ O → HOOCH ₂ S + CH ₂ O	1.0e6	(Saunders et al., 2003)
OOCCH ₂ SCH ₂ OOH + HO ₂ → HOOCH ₂ SCH ₂ OOH + O ₂	$1.13 \times 10^{-13} \exp(1300/T)$	(Saunders et al., 2003)
HPMTF + OH → HOOCH ₂ SCO + H ₂ O	1.11e-11	(Patroescu et al., 1996; Vermeuel et al., 2020)
HOOCH ₂ SCO → HOOCH ₂ S + CO	$9.2 \times 10^9 \exp(-505.4/T)$	(Wu et al., 2015)



$\text{HOCH}_2\text{SCO} \rightarrow \text{OH} + \text{CH}_2\text{O} + \text{OCS}$	$1.6e7 * \exp(-1468.6/T)$	(Wu et al., 2015)
$\text{HOCH}_2\text{S} + \text{O}_3 \rightarrow \text{HOCH}_2\text{SO} + \text{O}_2$	$1.15e-12 * \exp(430/T)$	(Saunders et al., 2003)
$\text{HOCH}_2\text{S} + \text{NO}_2 \rightarrow \text{HOCH}_2\text{SO} + \text{NO}$	$6.0e-11 * \exp(240/T)$	(Saunders et al., 2003)
$\text{HOCH}_2\text{SO} + \text{O}_3 \rightarrow \text{SO}_2 + \text{CH}_2\text{O} + \text{OH} + \text{O}_2$	$4.0e-13$	(Saunders et al., 2003)
$\text{HOCH}_2\text{SO} + \text{NO}_2 \rightarrow \text{SO}_2 + \text{CH}_2\text{O} + \text{OH} + \text{NO}$	$1.2e-11$	(Saunders et al., 2003)

201

202

203

Table 4. Overview of the MSA-producing branch of the H-abstraction pathway of DMS oxidation (Fung et al., 2022).

Gas-phase reactions	Rate (s^{-1})	Original References
$\text{DMS} + \text{OH} \rightarrow \text{MSP} + \text{H}_2\text{O}$	$1.12e-11 * \exp(-250/T)$	(Saunders et al., 2003)
$\text{DMS} + \text{Cl} \rightarrow 0.45\text{MSP} + 0.55\text{C}_2\text{H}_6\text{SCL} + 0.45\text{HCL}$	$3.40e-10$	(Fung et al., 2022)
$\text{C}_2\text{H}_6\text{SCL} \rightarrow \text{DMS} + \text{Cl}$	$9.00e1$	(Enami et al., 2004)
$\text{DMS} + \text{NO}_3 \rightarrow \text{MSP} + \text{HNO}_3$	$1.9e-13 * \exp(520/T)$	(Novak et al., 2021; Wollesen de Jonge et al., 2021)
$\text{MSP} + \text{NO} \rightarrow \text{CH}_3\text{SCH}_2(\text{O}) + \text{NO}_2$	$4.9e-12 * \exp(260/T)$	(Saunders et al., 2003)
$\text{MSP} + \text{MO}_2 \rightarrow \text{CH}_3\text{SCH}_2(\text{O}) + \text{O}_2$	$3.74e-12$	(Saunders et al., 2003)
$\text{CH}_3\text{SCH}_2(\text{O}) \rightarrow \text{CH}_3\text{S} + \text{CH}_2\text{O}$	$1.0e6$	(Saunders et al., 2003)
$\text{CH}_3\text{S} + \text{O}_3 \rightarrow \text{CH}_3\text{S}(\text{O}) + \text{O}_2$	$1.15e-12 * \exp(430/T)$	(Saunders et al., 2003)
$\text{CH}_3\text{S} + \text{O}_2 \rightarrow \text{CH}_3\text{S}(\text{OO})$	$1.20e-16 * \exp(1580/T)$	(Saunders et al., 2003)
$\text{CH}_3\text{S}(\text{O}) + \text{O}_3 \rightarrow \text{CH}_3(\text{O}_2) + \text{SO}_2$	$4.00e-13$	(Saunders et al., 2003)
$\text{CH}_3\text{S}(\text{OO}) \rightarrow \text{CH}_3(\text{O}_2) + \text{SO}_2$	$5.60e16 * \exp(-10870/T)$	(Saunders et al., 2003)
$\text{CH}_3\text{S}(\text{OO}) \rightarrow \text{CH}_3\text{SO}_2$	1.00	(Saunders et al., 2003)
$\text{CH}_3\text{SO}_2 + \text{O}_3 \rightarrow \text{CH}_3\text{SO}_3 + \text{O}_2$	$3.00e-13$	(Saunders et al., 2003)
$\text{CH}_3\text{SO}_2 \rightarrow \text{CH}_3(\text{O}_2) + \text{SO}_2$	$5.00e13 * \exp(-9673/T)$	(Saunders et al., 2003)
$\text{CH}_3\text{SO}_3 + \text{HO}_2 \rightarrow \text{MSA} + \text{O}_2$	$5.00e-11$	(Saunders et al., 2003)
$\text{CH}_3\text{SO}_3 \rightarrow \text{CH}_3(\text{O}_2) + \text{H}_2\text{SO}_4$	$5.00e13 * \exp(-9946/T)$	(Saunders et al., 2003)

204

205

206

207

208

To examine the sensitivities of size-resolved aerosol formation and growth to DMS chemistry modifications, model simulations are conducted as summarized in Table 5. Output from simulations MOD and MOD_noHetLossHPMTF was then compared against simulation BASE to understand the contribution of these additional chemical reactions on spatial pattern of the surface concentration of major oxidation products of DMS.

209

Table 5. List of mechanisms used in GEOS-Chem-TOMAS simulations.

Model Runs	Mechanism	HPMTF Cloud Loss*	HPMTF Aerosol Loss [#]
BASE	All reactions from Table 1	-	-
MOD_noHetLossHPMTF	All reactions from Table 2-4	Off	Off
MOD	All reactions from Table 2-4	On	On

210

211

*HPMTF cloud loss: $\text{HPMTF} = \text{SO}_4^{2-}$ (activity co-efficient, $\gamma = 0.01$), HPMTF aerosol loss: $\text{HPMTF} = \text{SO}_4^{2-}$ ($\gamma = 0.001$)

212

213

As shown in Table 2, the modified DMS chemistry simulations examined here include gas- and aqueous-phase oxidation of DMS and its intermediate oxidation products by OH, NO₃, O₃, and



214 halogenated species as previously explored in an older version of GEOS-Chem (Chen et al., 2018).
215 The aqueous-phase reactions in cloud droplets and aerosols were parameterized assuming a first-
216 order loss of the gas-phase sulfur species (Chen et al., 2018). Further building upon this previous
217 mechanism, the scheme used here also includes the formation and loss of HPMTF as previously
218 tested in the global climate model CAM6-Chem as shown in Table 3 (Veres et al., 2020). Table 4
219 presents the third piece of the mechanism: a gas-phase MSA-producing branch of the H-abstraction
220 pathway in the DMS chemistry bridging the other two sets of the reactions (Fung et al., 2022). A
221 similarly integrated mechanism (Table 2-4) has been previously explored using the CAM6-Chem
222 model with a focus on radiation budget impacts, with the exception of the $\text{DMS} + \text{NO}_3 = \text{MSP} +$
223 HNO_3 reaction (included in Table 4) considered in this work (Fung et al., 2022; Novak et al., 2021;
224 Wollesen de Jonge et al., 2021). We use a rate constant of $1.11 \times 10^{-11} \text{ cm}^3 \text{ molecules}^{-1} \text{ s}^{-1}$ for
225 $\text{HPMTF} + \text{OH}$, which is an experimentally determined OH-oxidation rate of methyl thioformate
226 (MTF; CH_3SCHO ; a structurally similar proxy to HPMTF) (Vermeuel et al., 2020). An exploration
227 of reaction rate uncertainty for the HPMTF+OH reaction (Table 3), including both high and low
228 end limits of $5.5 \times 10^{-11} \text{ cm}^3 \text{ molecules}^{-1} \text{ s}^{-1}$ and $1.4 \times 10^{-12} \text{ cm}^3 \text{ molecules}^{-1} \text{ s}^{-1}$ resulted in
229 only minor impacts on the fate of HPMTF and ultimate sulfate formation in our simulations
230 (Novak et al., 2021; Wu et al., 2015).

231 Model sensitivity simulations were also performed with (case “MOD”) and without HPMTF
232 heterogeneous uptake to clouds and aerosols (case “MOD_noHetLossHPMTF”) to account for
233 how much of the DMS-derived HPMTF eventually forms SO_2 in the presence of these additional
234 loss processes (Table 5). Previous work shows that aerosol surface chemistry causes additional
235 decreases in HPMTF mixing ratios, primarily over land, and that the loss of HPMTF in clouds is
236 larger (36%) than losses from aerosols (15%) when using an uptake coefficient of $\gamma = 0.01$ for both
237 processes (Novak et al., 2021). In this work, based on recent laboratory measurements, we use a
238 smaller uptake coefficient ($\gamma = 0.001$) for HPMTF loss to aerosols (Table 5) (Jernigan et al.,
239 2022b). We assume HPMTF directly produces sulfate in cloud and aerosol followed but previous
240 work even though there is uncertainty in the fate of HPMTF heterogeneous loss (Zhang and
241 Millero, 1993; Novak et al., 2021; Jernigan et al., 2022a).

242 All simulations are conducted for the year 2018, which was chosen to match the model simulation
243 with the dates of the NASA Atmospheric Tomography flight campaign (ATom-4) offering
244 observational data for HPMTF and DMS. Rate coefficients for all gas-phase sulfur reactions are
245 obtained from the most recent JPL report and other references while sulfur product yields for gas-
246 phase reactions are obtained from various laboratory and modeling studies (Burkholder et al.,
247 2020; Lucas and Prinn, 2002; Hoffmann et al., 2016; Gershenson et al., 2001; Kowalczyk et al.,
248 2003; Zhou et al., 2019). The simulations included sea salt debromination except for some
249 sensitivity tests described below (Zhu et al., 2019; Schmidt et al., 2016).

250 We note that previous work has explored the impact of MSA on aerosol growth, including
251 modifications within TOMAS to represent this process (Hodshire et al., 2019). We do not include
252 this process here. Future work is recommended to examine its importance in the context of the
253 chemistry updates presented here.



254 **3 Result and discussion**

255 3.1 DMS burden and oxidation pathways

256 We find that the global burden of DMS in the MOD simulation is 56 Gg S, 51% lower than what
 257 we find with the simulation BASE (108 Gg S). Even with this 48% reduction, global burdens are
 258 still well within the range of 9.6–150 Gg S suggested in other studies (Faloona, 2009; Kloster et
 259 al., 2006). Figure 2a shows that surface DMS mixing ratios are highest in the North Pacific and
 260 North Atlantic oceans for June-July-August (JJA) and in the Southern Ocean during the months
 261 of December-January-February (DJF), revealing the underlying seasonality of DMS emissions.
 262 According to previous studies, the highest DMS concentrations usually occur in summer months
 263 due to higher rates of primary production in the presence of adequate solar irradiation and high
 264 temperatures for both hemisphere (Galí et al., 2018; Lana et al., 2011; Wang et al., 2020). In
 265 simulation MOD, the global mean surface-layer DMS burden was higher in SH for DJF and lower
 266 in NH for JJA which is due to larger ocean area in the SH than NH. We also find that the reactions
 267 of this expanded DMS oxidation mechanism collectively contribute to reductions in mean surface-
 268 layer DMS concentration of 55% and 20% compared to BASE for JJA and DJF respectively (Fig.
 269 2b). These reductions are due primarily to the addition of multiple new chemical loss pathways
 270 compared to BASE, which are especially impactful during JJA months due to elevated BrO
 271 in the SH winter and also higher O₃ and OH concentration in the NH summer compared to the SH
 272 summer (Zhang et al., 2018; Pound et al., 2020).

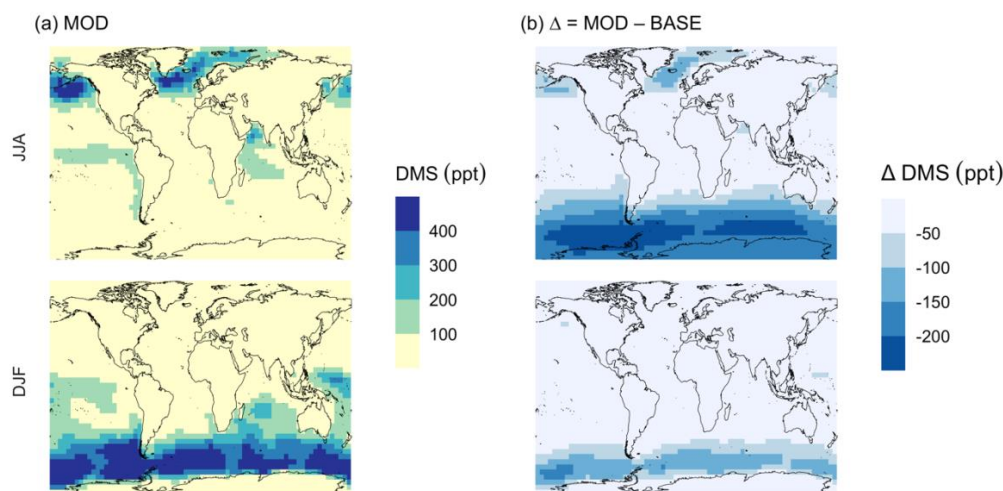


Figure 2 Geographic distribution of mean surface DMS mixing ratio (ppt) for simulation (a) MOD and (b) difference between simulations from its baseline, $\Delta = \text{MOD} - \text{BASE}$ from GEOS-Chem simulations. Here, JJA and DJF represent June-July-August and December-January-February respectively. Simulations are described in Table 5.

273 As shown in Fig. 2b, this DJF DMS reduction is seen mainly over the Southern Ocean and is
 274 largely attributable to faster chemical losses through the added reactions of $\text{DMS} + \text{BrO}$ and
 275 $\text{DMS}_{(\text{aq})} + \text{O}_{3(\text{aq})}$, which in earlier work was hypothesized as a possible reason for high model biases
 276 in the absence of detailed halogen chemistry (Chen et al., 2016). The global lifetime of DMS
 277 decreases from 1.5 days in the BASE simulation to 1.2 days in the MOD simulation.



278 These values are comparable to the range of 0.8–2.1 d reported by previous studies (Chen et al.,
279 2018; Fung et al., 2022).

280 In the BASE simulation the chemical loss of DMS acts as its only sink (as opposed to dry and wet
281 deposition), leading to a full conversion yield of DMS into SO₂ (82.5%) and MSA (17.5%). Figure
282 3 shows that in simulation MOD with updated DMS oxidation scheme DMS is mainly oxidized
283 by OH in the gas phase, with 32.1% of losses proceeding via the H-abstraction channel and 28.4%
284 via the OH-addition pathway, together contributing up to 60% of global average loss with high
285 regional contribution over the tropical oceans via the abstraction channel where surface OH is the
286 highest. NO₃ oxidation of DMS accounts for another 15.8% of global DMS chemical losses via
287 two possible oxidation pathways. NO₃ loss pathways are strongest in the Northern Hemisphere
288 mid-latitudes near coastal regions near high NO_x sources, consistent with previous studies (Chen
289 et al., 2018; Fung et al., 2022). Oxidation by BrO is responsible for 18.5% of the global DMS
290 removal, falling within the previously estimated range of 8%–29% (Boucher et al., 2003; Khan
291 et al., 2016; Chen et al., 2018). Regionally, its contribution can reach 50%–60% over high latitudes
292 of the Southern Hemisphere as well as to the north near the Arctic Ocean, consistent with previous
293 box model studies based on the availability of high BrO and low OH and NO₃ for those regions
294 (Hoffmann et al., 2016). DMS + O₃ accounts for 2.7% (aqueous) and 0.7% (gas phase) of global
295 surface DMS loss. The higher contribution from BrO and lower from O₃ using this mechanism
296 compared to some previous studies could be explained in part by the recently implemented sea-
297 salt debromination mechanism in GEOS-Chem, resulting in a much higher background level of
298 BrO as well as lower O₃ abundance, especially in the southern hemisphere (Boucher et al., 2003;
299 Chen et al., 2018; Fung et al., 2022; Sherwen et al., 2016a; Wang et al., 2021). To further quantify
300 the importance of the sea salt debromination mechanism, we perform an emissions sensitivity test
301 by turning this emission source off while using updated MOD chemistry (Fig. A1). As would be
302 expected, these simulations show much lower BrO formation and resulting chemical impacts, with
303 overall oxidation contributions comparable to previous literature (Schmidt et al., 2016; Wang et
304 al., 2021). We find that under this scenario the relative contribution of BrO for DMS loss decreases
305 to 3.6%, while the DMS + O₃ pathway increases to 3.7% (aqueous) and 1.1% (gas phase), and the
306 DMS + OH pathway increases to 36.4% (abstraction) and 34.7% (addition) of global surface DMS
307 loss (Fig. A1). The DMS loss via interaction with NO₃ also increases by 2.7% total for the two
308 loss processes present in the mechanism. The relative contributions of other oxidants remain
309 mostly unaffected in the BrO sensitivity test.
310

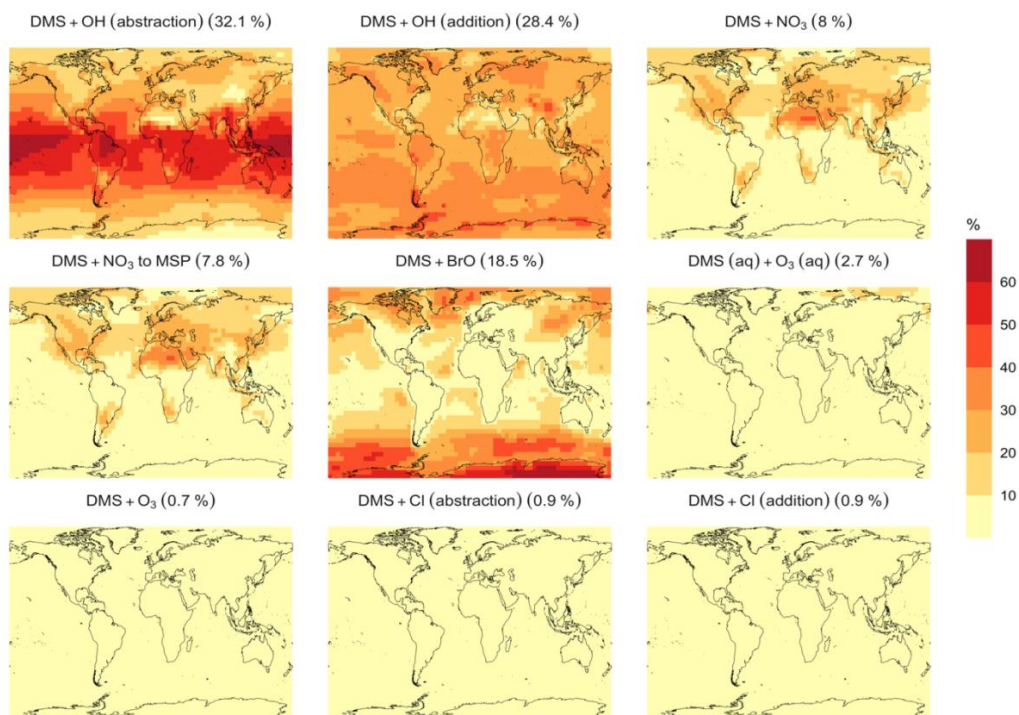


Figure 3 Geographic distribution of the annual mean, surface layer fraction of total DMS oxidation (percent) attributed to different tropospheric oxidants for simulation MOD (described in Table 5). Percentages in parentheses indicates average contribution to global chemical loss.

311 Regionally, the fractional contribution of aqueous-phase DMS + O₃ to DMS oxidation can be up
 312 to 10%–20% over high-latitude oceans, which is in the middle of the 5%–30% contribution to
 313 high-latitude DMS losses previously reported (Chen et al., 2018; Fung et al., 2022; von Glasow
 314 and Crutzen, 2004). The Cl oxidation reactions via the addition or abstraction channels each
 315 contribute about 0.9% (with and without sea salt debromination) to the chemical removal of DMS,
 316 consistent with some previous studies (Atkinson et al., 2004; Fung et al., 2022). This does differ
 317 from other reported values however, including those from a global model study (4%) and box
 318 model simulations (8%–18%) (Chen et al., 2018; Hoffmann et al., 2016; von Glasow and Crutzen,
 319 2004). It's worth noting that none of the studies reporting such high Cl contributions included
 320 HPMTF formation and loss. Ongoing uncertainties associated with model-observation bias of Cl
 321 should be further resolved to get better representation of halogenated species contributions to DMS
 322 loss (Wang et al., 2021).

323 3.2 Model-Observations Comparison

324 The surface mixing ratio of HPMTF for May 2018 is plotted in Figure 4 and compared with the
 325 observational measurement of HPMTF made during the ATom-4 mission during the NASA DC-
 326 8 flight campaign, which sampled the daytime remote marine atmosphere over the Pacific and
 327 Atlantic Oceans. The ATom-4 measurements were carried out during daytime hours between April
 328 24 and May 21, 2018 for 21 non-continuous days.



329 For this campaign, flight patterns covered vertical profiles from 0.2 to 14 km above the ocean
 330 surface. The flight leg duration was 5 minutes and boundary layer altitude of 150 to 200 m above
 331 the ocean surface. Since most of these measurement days are within the month of May 2018, here
 332 we initially compare observations with modeled output of mean surface concentration of HPMTF
 333 for this month. With the rate of isomerization reaction used in previous work, we find regional
 334 high bias in HPMTF mixing ratios in the northern hemisphere (Veres et al., 2020). These
 335 occurrences could be due to high DMS emission in these regions. Overall though we find that the
 336 modified GEOS-Chem simulation results in better agreement for global surface layer HPMTF
 337 levels compared to previous modeled approaches using the CAM-chem model, which showed even
 338 higher biases (Veres et al., 2020).

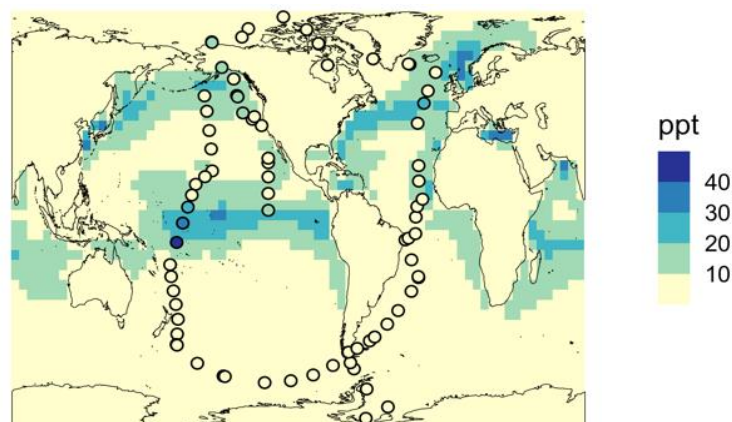


Figure 4 Geographic distribution of May 2018 monthly mean surface-layer mixing ratio of HPMTF for simulation MOD mechanism represented for May 2018. The circles represent measurements of HPMTF during the ATom-4 mission by NASA DC-8 flight tracks with a limit of detection <1 ppt.

339 We further evaluate model output through a comparison with ATom-4 aircraft observations for
 340 specific days of measurement as shown in Figure 5. For this comparison, the model is sampled at
 341 the time and location of aircraft measurements by ATom-4 using the planeflight diagnostic of
 342 GEOS-Chem.

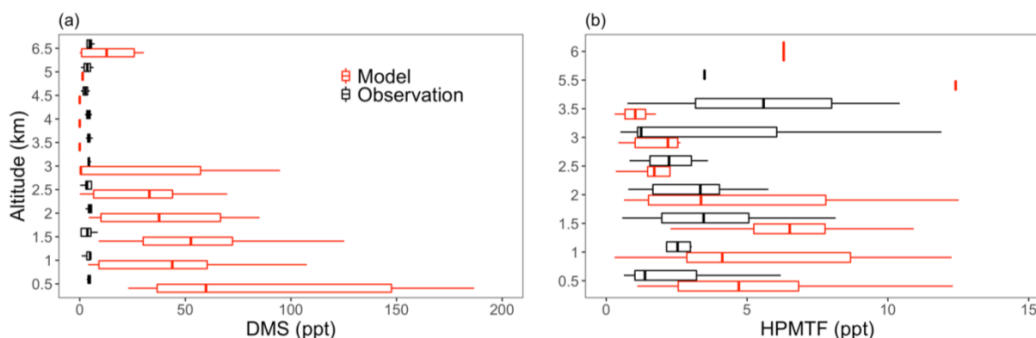


Figure 5 Vertical profiles of (a) DMS and (b) HPMTF mixing ratios from ATom-4 observations (black) and model with simulation MOD sampled along the ATom-4 flight tracks (red, simulations are described in Table 5) binned every 0.5 km of flight distance. Box plot whiskers show full range of distribution at each altitude bin. DMS observations are from Whole Air Samples (WAS) while HPMTF DC-8 observations are at 1 Hz.



343 DMS concentrations measured during ATom-4 by whole air sampler (WAS) and modified
344 chemistry simulation values for nearest neighbor grid cells are shown in Figure 5a across different
345 altitude. Modeled surface DMS concentrations are significantly higher than those observed during
346 ATom-4 missions especially close to the surface. However, modeled concentrations decrease
347 rapidly at higher altitudes, resulting in slightly lower concentration compared to observations.
348 Even with this near surface bias, simulation MOD relative to BASE has greater DMS losses and a
349 shorter DMS lifetime (from 1.5 d to 1.2 d), reducing the model bias compared to simulation BASE.
350 The reduction in modeled DMS is largest over the Southern Ocean where oxidation by BrO and
351 O₃ in the aqueous phase plays the major role in reducing DMS concentration, thereby reducing the
352 model-observation bias (Fig. 2b). Remaining model biases could be at least partially attributed to
353 variability in DMS emissions themselves as well as model errors in oxidant concentrations and
354 cloud cover.

355 For HPMTF, Figure 5b shows that in most of the cases observed and modeled HPMTF
356 concentrations (from MOD) remain below 15 ppt. Agreement between individual observations and
357 modeled HPMTF mixing ratios in the vertical profile (Fig. 5b) is modest, but spatial patterns of
358 mean surface-layer concentrations are generally well captured (Fig. 4). We also find that the
359 modeled HPMTF:DMS ratios range from 0.2:1 to 0.5:1 on a daily basis, compared to 0.5:1
360 observed during ATom-4 using the calibration maintained during measurement, implying
361 reasonably good agreement for this value over daily time scales (Veres et al., 2020). Lower ratios
362 have also been observed under certain meteorological conditions, where SARP flight campaign
363 data shows much lower HPMTF:DMS ratios (< 0.2) on cloudy days (Novak et al., 2021). The
364 existing biases in these results could be explained by either model underestimates in the DMS-to-
365 HPMTF conversion via gas-phase oxidation, or overestimates in HPMTF cloud loss and aerosol
366 uptake. Our simulations suggest that cloud loss is the dominant removal process of HPMTF, as
367 shown previously while gas-phase OH oxidation plays a minor role (Novak et al., 2021). Thus, the
368 addition of cloud uptake dramatically decreases HPMTF concentrations, potentially reducing the
369 model-observation bias in the lower troposphere, despite having high DMS concentrations relative
370 to previous studies. Overall, this allows only 6% of HPMTF produced to end up as SO₂ with about
371 83% lost to clouds and thus removed from the system, resulting net reduction in mean global SO₂
372 by about 38%. Previous work focusing entirely on gas-phase and heterogeneous loss of HPMTF
373 shows a much higher bias for both DMS and HPMTF during cloudy and clear sky conditions using
374 the same model and a condensed DMS oxidation mechanism, indicating that the addition of gas-
375 phase and heterogeneous oxidation of DMS including additional intermediates such as DMSO and
376 MSIA further reduce model biases for HPMTF (Fig. 5b) (Novak et al., 2021).

377 We also compare the modeled DMS mixing ratio averaged for each month with the observational
378 data collected at Crete Island (35° N, 26° E) (Kouvarakis and Mihalopoulos, 2002; Chen et al.,
379 2018). Comparing simulations BASE and MOD, we find a closer match with DMS observations
380 for simulations using modified DMS chemistry. Modeled DMS mixing ratios calculated using base
381 chemistry show strong positive bias during the months of May and June. By comparison, during
382 the same period the modeled DMS mixing ratios calculated with modified chemistry reduces the
383 bias from 102% to 44%. One of the reactions that plays a significant role in reducing this bias is
384 DMS + BrO, which as indicated earlier is responsible for faster chemical loss of DMS, especially
385 in the southern hemisphere high latitudes.

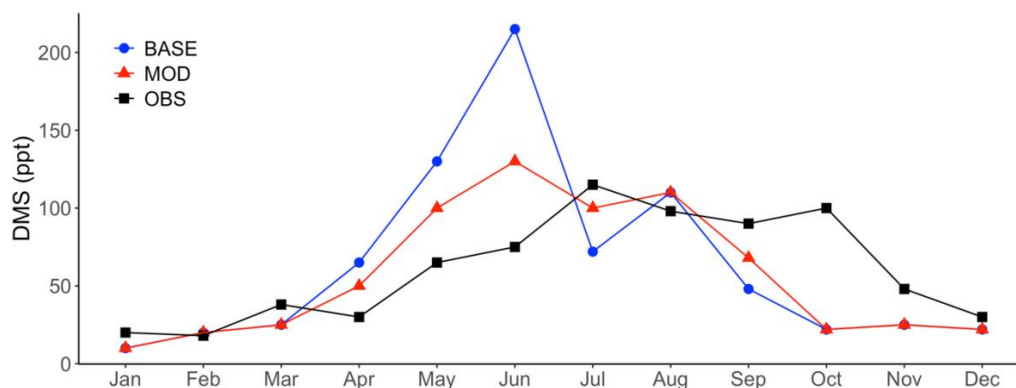


Figure 6 Observed (OBS) monthly mean surface DMS mixing ratios at Crete Island and for simulations BASE and MOD. Simulations are described in Table 5.

386

387

3.3 Implications of the extended DMS oxidation mechanism

388

389

390

391

392

393

394

395

396

397

398

399

Figure 7 shows that the MOD simulation results in 37% reduction of SO_2 relative to BASE, but a huge increase in SO_4^{2-} in most regions. These changes suggest that the combination of gas-phase and aqueous-phase reactions results in a higher net yield of MSA and HPMTF and a lower net yield of gas-phase SO_2 . Additionally, comparison of simulation MOD relative to MOD_noHetLossHPMTF (Fig. A2a) shows that loss of HPMTF in cloud droplets and aerosol reduces the global mean production of SO_2 by 14.7%, contributing to the SO_2 reduction and increasing mean surface layer sulfate by 16% (Fig. A2b). This reduction in SO_2 is expected to reduce the availability of gas-phase sulfuric acid for new particle formation by nucleation (Clarke et al., 1998a). Total SO_4^{2-} increases over the ocean, however, because the increased SO_4^{2-} production from rapid loss of MSA and HPMTF in aqueous-phase offsets the reduced oxidation of SO_2 (Fig. 7b).

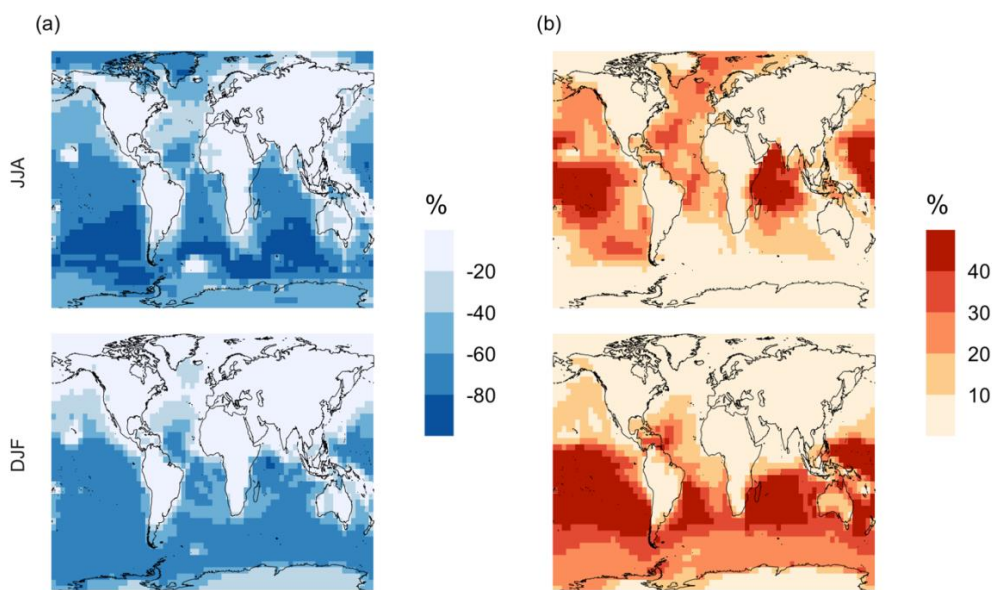


Figure 7 Percent change in simulated surface layer (a) SO₂ and (b) SO₄²⁻ for simulation MOD relative to BASE for June, July and August mean (JJA) and December, January, and February mean (DJF). Simulations are described in Table 5.

400 Qualitatively, the regions showing the highest percent changes of SO₂ are consistent with previous
 401 studies that included HPMTF chemistry and loss processes though the extent of this reduction is
 402 much higher with the integrated mechanism used in our study (Fig. 7a) (Novak et al., 2021). The
 403 regions with the largest percent change in SO₂ reduction are those where DMS oxidation
 404 contributes most to SO₂, and where HPMTF production and in-cloud oxidation of HPMTF are
 405 efficient. This spatial pattern thus helps us to identify where the production and heterogeneous loss
 406 of HPMTF and MSA is enhanced. Even though the cloud loss of HPMTF increases the production
 407 of surface sulfate, the total global sulfate burden we calculate increases by only 4% from the BASE
 408 sulfate burden of around 575 Gg S. This can be attributed to minor contribution of DMS and its
 409 intermediate oxidation products in SO₂ production compared to other non-DMS derived sources.
 410 In addition, the production of stable intermediate oxidation products delay the conversion of SO₂
 411 to SO₄²⁻ and modify its spatial distribution in the marine environment. Thus, we should expect
 412 these aqueous phase oxidation products to contribute to particle mass rather than increase the
 413 number of nucleated particles, as suggested in other studies (Clarke et al., 1998b; Novak et al.,
 414 2021; Williamson et al., 2019).

415
 416

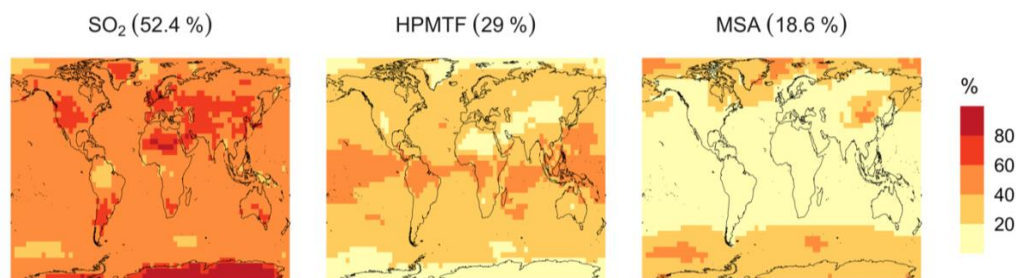


Figure 8 Simulated branching ratio (in %) of the DMS oxidation mechanism considering SO₂, HPMTF and MSA as major terminal oxidation products calculated from their annual total production rate for simulation MOD.

417 The spatial distribution of product branching ratios of DMS oxidation is shown in Figure 8. Here,
 418 29% of the annual total DMS oxidation will end up as HPMTF, while final SO₂ yield decreases to
 419 52.4% compared to 82.5% for the BASE simulation (Fig. A3a). The terminal HPMTF branch
 420 represents sulfur removed from the system by cloud and aerosol uptake of HPMTF, leading to a
 421 reduced overall formation of SO₂. With sea salt debromination turned off, modified chemistry
 422 forms even more HPMTF (32.5%), slightly higher SO₂ (56%), and lowers the yield of MSA to
 423 11.5%, underscoring the importance of halogen chemistry for MSA production (Fig. A3b). These
 424 results are broadly consistent with observationally constrained estimates from ATom-4 flight
 425 campaigns, where ~ 30% - 40% DMS was oxidized to HPMTF along their flight tracks compared
 426 to 32.8% for the full branch of HPMTF in the present work, as well as with previous modeling
 427 studies showing 33% HPMTF formation as terminating product (Veres et al., 2020; Fung et al.,
 428 2022). MSA is produced mostly by aqueous phase oxidation of MSIA by O₃ and OH according to
 429 the mechanism used here and has high abundance near the Southern Ocean and Antarctic belt as
 430 reported by previous studies (Chen et al., 2018; Hoffmann et al., 2016; Fung et al., 2022). The
 431 global burden of MSA decreases dramatically, from 19 Gg S for ‘Base’ to 8.6 Gg S for ‘All’
 432 chemistry. The higher rate of major loss process or lower rate of production of MSA from the
 433 aqueous phase reactions could be responsible for this reduction in global budget (Fung et al., 2022).

434 3.4 Impact on aerosol size distributions

435 Following the percent change in simulated surface layer SO₂ and SO₄²⁻ for modified DMS
 436 chemistry (Fig. 7), we further explore how this expanded DMS oxidation chemistry impacts
 437 modeled aerosol size distributions. Figure 9 shows the global mean surface-layer percent change
 438 in the normalized aerosol number concentration for modified chemistry relative to the BASE
 439 simulation, with and without cloud and aerosol HPMTF loss processes. The aerosol number
 440 concentration decreases for the sub-80 nm diameter size bins for both simulations, especially
 441 during the DJF months when cloud and aerosol loss pathways of HPMTF are included (MOD
 442 case), demonstrating the negative impact of these processes on simulated new particle formation.
 443 Without these processes included (as in case MOD_noHetLossHPMTF), percent changes are far
 444 more modest for these smaller size ranges. On the other hand, HPMTF lost to clouds and aerosols
 445 increases the simulated number of particles with diameter above 100 nm in the MOD simulation,
 446 consistent with the increase in sulfate mass concentrations shown in Fig. 7 and suggesting that
 447 HPMTF heterogeneous loss promotes simulated particle growth to diameters larger than 80-100
 448 nm. The greater abundance of particles larger than 100 nm also acts as a condensation sink, further
 449 suppressing nucleation and growth at smaller size ranges.

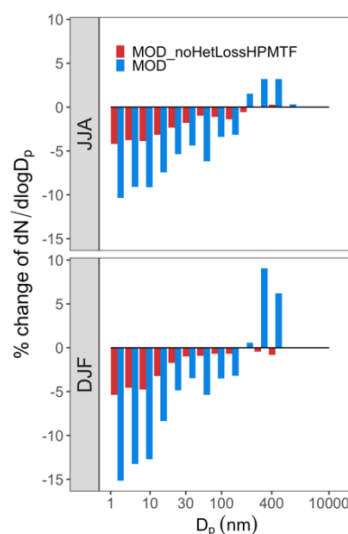


Figure 9 Global mean surface-layer percent change in normalized aerosol number concentration for different size bins with particle diameter, D_p in the range of $3 \text{ nm} < D_p < 10000 \text{ nm}$ for simulations MOD and MOD_noHetLossHPMTF relative to simulation BASE. Simulations are described in Table 5.

450 The geographic distribution of surface layer aerosol number concentration for aerosol in the size
 451 range of 3 – 80 nm for two seasons is shown in Figure 10. We find that global mean aerosol number
 452 concentration in this size range decreases for simulations MOD and MOD_noHetLossHPMTF
 453 relative to BASE by 12% and 9.7% respectively. Decreases are greater for simulation MOD (Fig.
 454 10b). Fig. 10c shows the effect of HPMTF heterogenous loss processes on the number of particles
 455 with diameters between 3-80 nm for simulation MOD relative to simulation
 456 MOD_noHetLossHPMTF. The largely negative impact of HPMTF loss to clouds and aerosols on
 457 sub-80 nm particle number is contributed to by enhanced direct sulfate formation on pre-existing
 458 particles, bypassing gas-phase SO_2 formation (a precursor for new particle formation). As well, in
 459 the model, new particles grow through condensation of H_2SO_4 and organics and their growth are
 460 dependent on the condensation sink, while loss of particle number depends on the coagulation
 461 sink. Thus, changes to the condensation/coagulation sinks and sulfuric acid production rate
 462 through the updated mechanism will also alter the growth rates of small particles (sub-80 nm) as
 463 well as their coagulation loss rates. Hence, similar to the discussion for Figure 9, the reduction of
 464 gas-phase production of H_2SO_4 in MOD relative to BASE slows new-particle formation and
 465 growth, while the additional production of sulfate through aqueous chemistry on larger particles
 466 in MOD increases the coagulation scavenging of the newly formed particles. These two effects
 467 synergistically reduce the concentration of ultrafine particles in the model. The sensitivity of these
 468 results to the new sea salt debromination parameterization is shown in Fig. A4, where we find a
 469 regional increase in aerosol number concentration at mid to higher latitude of the SH despite low
 470 BrO concentrations (Fig A4).

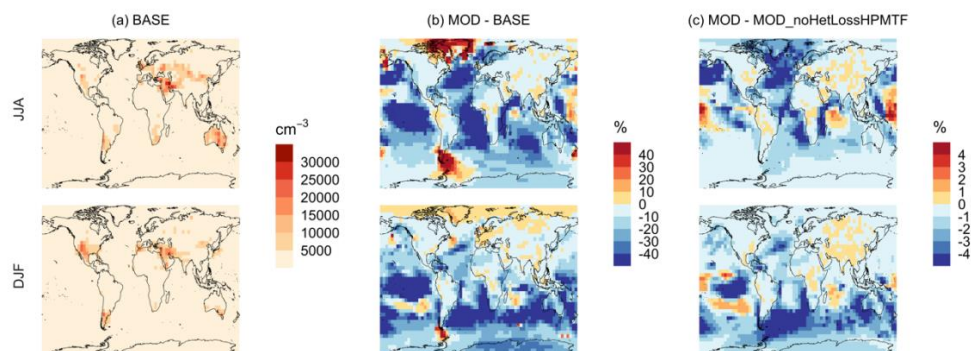


Figure 10 Geographic distribution of seasonal-mean surface-layer aerosol number concentration in cm^{-3} (for particles with diameters between 3 – 80 nm) for (a) the BASE simulation, (b) the percent difference between MOD and BASE and (c) the percent difference between MOD and MOD_noHetLossHPMTF to show the role of cloud and aerosol loss of HPMTF. Simulations are described in Table 5.

471

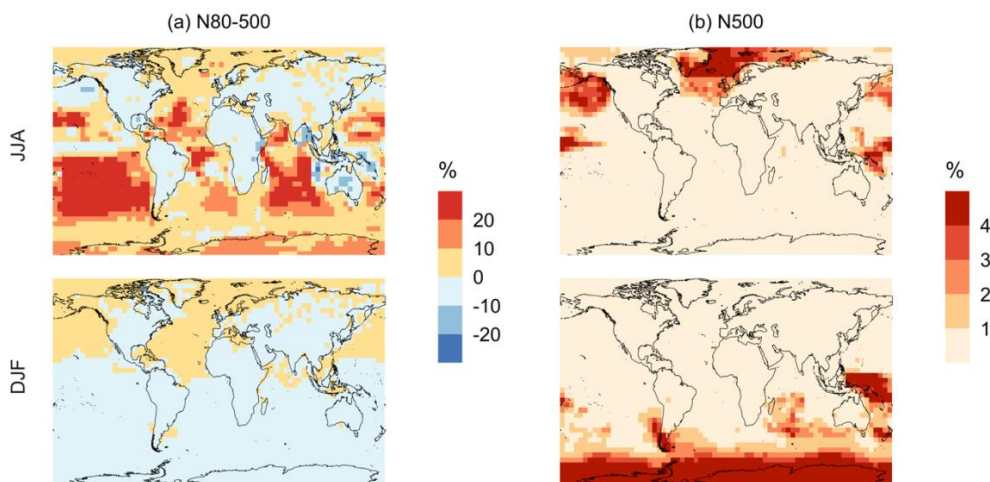


Figure 11 Geographic distribution of percent difference in seasonal-mean surface-layer aerosol number concentration in cm^{-3} for simulations MOD relative to simulations BASE for diameters between (a) 80 – 500 nm and (b) >500 nm. Simulations are described in Table 5.

472 Finally, we also analyze the impact of this expanded DMS scheme on particles larger than 80 nm
 473 (Fig. 11). We find increases of around 6.4% for JJA mean surface layer number concentration of
 474 aerosol with diameters between 80-500 nm, while DJF months show mean reductions of -7.9% for
 475 DJF despite largely positive changes in the marine NH for these months (Fig. 11a). However, for
 476 the > 500 nm size ranges (Fig. 11b), the global mean surface layer number concentration of aerosol
 477 mostly increases, with highest changes occurring in the areas of peak DMS emission in both
 478 hemispheres, during their summertime season. A similar trend is observed in the absence of cloud
 479 and aerosol HPMTF uptake in simulation MOD_noHetLossHPMTF (Fig. A5).



480 Comparing the regional extent and direction of this change, we find the net increase in particle
481 number concentration is higher for MOD compared to MOD_noHetLossHPMTF, highlighting the
482 importance of HPMTF loss processes to clouds and aerosols as a contributor of CCN.
483



484 4 Conclusion

485 In this study we update the default DMS oxidation scheme in the GEOS-Chem model by
486 implementing an integrated oxidation mechanism. The new scheme includes gas-phase and
487 aqueous phase reactions involving DMSO, MSIA and HPMTF formation, as well as newly
488 identified HPMTF loss processes yielding considerable changes in seasonal concentrations of
489 major oxidation products and sulfur-derived aerosols. With this new chemistry scheme, DMS
490 concentration decreases by 48% relative to the BASE scheme in GEOS-Chem globally due to the
491 presence of additional loss processes in the integrated mechanism reducing the bias to ATom-4
492 DMS measurement.

493 In this new scheme, OH, BrO, O₃ and NO_x species act as important sinks of DMS contributing to
494 60.5%, 18.5%, 3.4% and 15.8% global annual mean surface DMS loss, highlighting the relative
495 importance of these loss process in determining surface DMS budget. We also find that at higher
496 latitudes, gas phase and multiphase oxidation of DMS by O₃ and BrO becomes important to
497 determine the budget of DMS. On the other hand, at lower latitudes OH contribute to a greater
498 extent compared to other sinks and at comparable extent to previous studies exploring this
499 chemistry. For the global distribution of simulated HPMTF, our updated scheme in GEOS-Chem
500 provides a reduced high bias against observations compared to previous studies. While emissions
501 of BrO are uncertain in this version of GEOS-Chem, we find that the compound acts as a key sink
502 of DMS, especially over the Southern Ocean. Overall, we find large reduction in SO₂ (38%) and
503 an increase in sulfate (16%) due to the addition of heterogeneous HPMTF loss processes.

504 The lower SO₂ with the new DMS chemistry scheme contributes to a reduction in the global annual
505 mean surface layer number concentration of particles with diameters less than 80 nm by 12%,
506 contributed to by reductions in gas-phase precursors for new particle formation. There is a
507 concurrent increase of 4.5% in the global annual mean number of particles with diameters larger
508 than 80 nm. This latter global mean particle number change varies in sign seasonally, with a 6.4%
509 increase for JJA, and a 7.9% decrease for DJF. This decrease is dominated by southern hemisphere
510 summertime changes, connected with suppressed new particle formation/growth and enhanced
511 coagulation following additional sulfate production through aqueous chemistry, Cloud loss
512 processes related to HPMTF make key contributions to these simulated changes through
513 enhancement of aqueous-phase particle growth of those particle large enough to act as CCN.

514 Although the increased chemical mechanism complexity described in this work will necessarily
515 increase model computational cost (MOD simulation run times increase by approximately 16%),
516 this study highlights the value of including a more realistic chemical oxidation mechanism of DMS
517 and its stable intermediates for better representation of DMS-derived aerosol in the marine
518 atmosphere, as well as its seasonal size distributions. A reduced form of the key chemical species
519 and pathways should be able to capture the key processes with less computational impact and will
520 be a priority in future work.



521 **Appendix A: Additional figures**

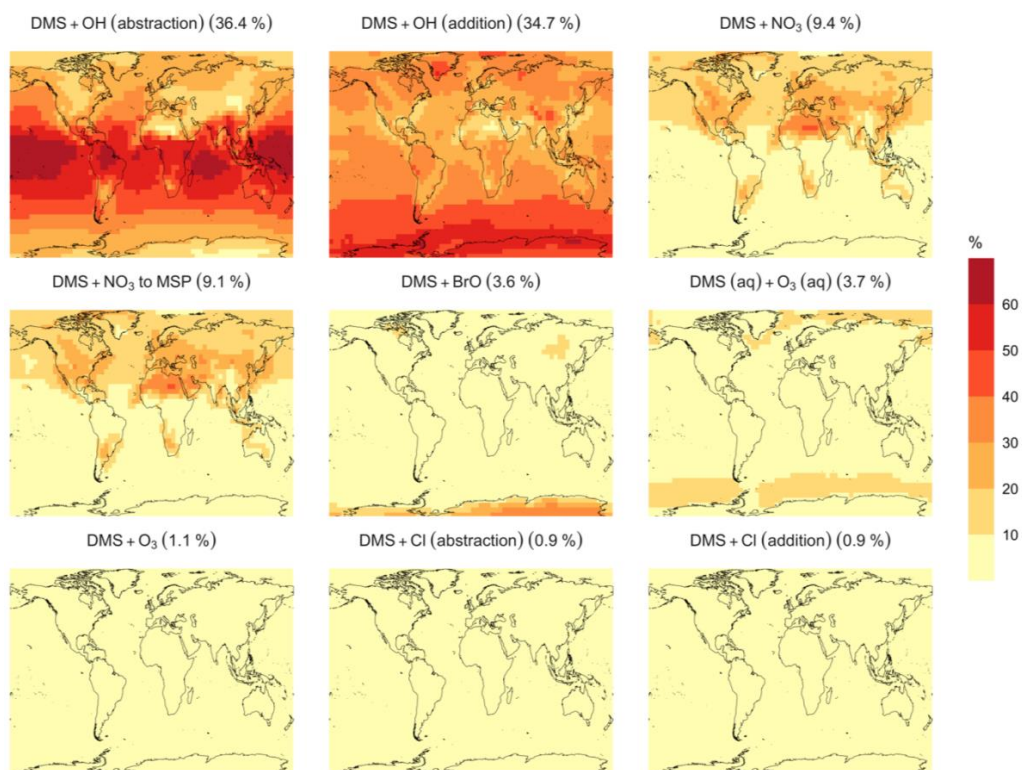


Figure A1 Surface layer geographic distribution of the simulated annual mean fraction of total DMS oxidation (percent) attributed to different tropospheric oxidants for a simulation otherwise the same as simulation MOD except with no sea salt debromination. Percentages in parentheses indicate global average contribution to chemical loss. Simulations are described in Table 5.

522

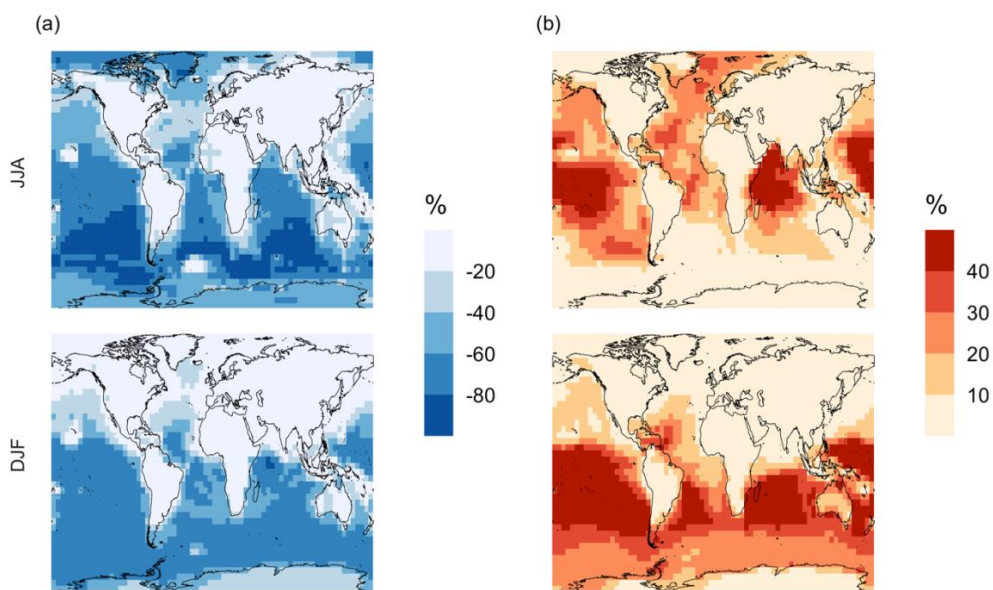


Figure A2 Percent change in simulated surface layer (a) SO₂ and (b) SO₄²⁻ for simulation MOD relative to MOD_noHetLossHPMTF for June, July and August mean (JJA) and December, January, and February mean (DJF). Simulations are described in Table 5.

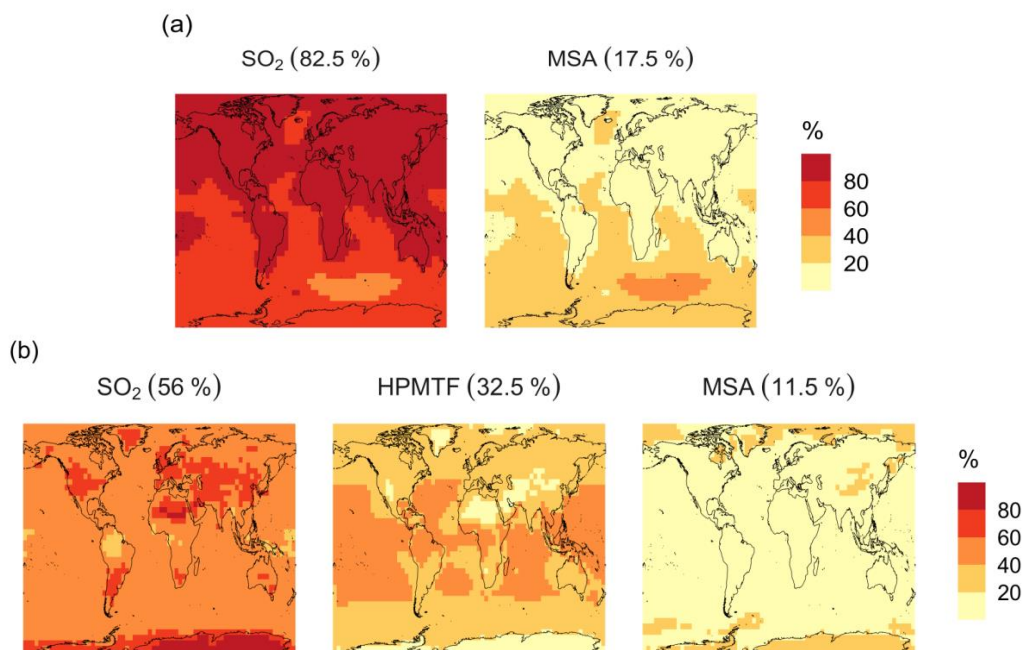


Figure A3 Simulated annual mean surface layer branching ratios (in %) of the DMS oxidation mechanism considering SO₂, HPMTF, and MSA as major oxidation products calculated from their total production rates for simulations similar to (a, top row) BASE and (b, bottom row) MOD, except all with no sea salt debromination. Simulations are described in Table 5.

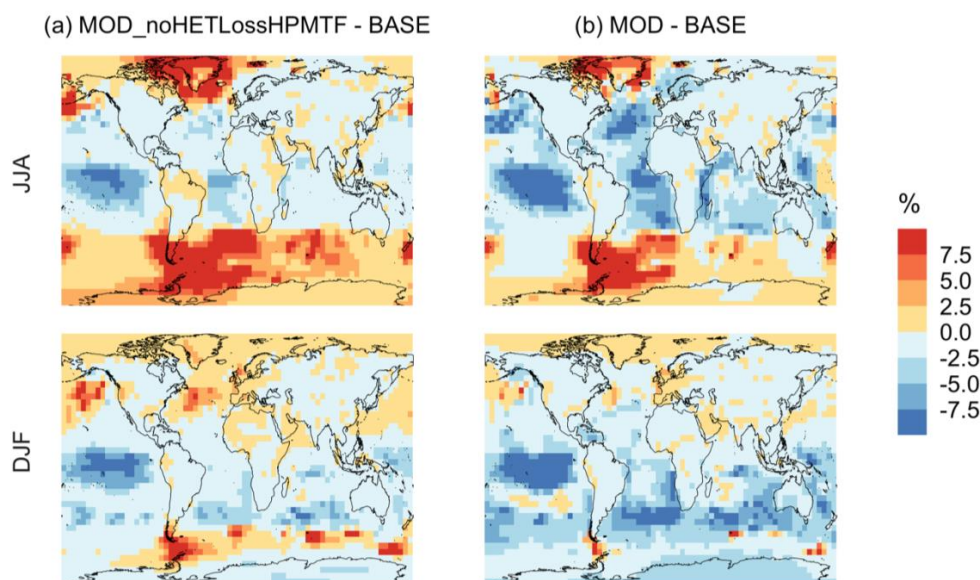


Figure A4 Geographic distribution of percent difference in seasonal-mean surface-layer aerosol number concentration in cm^{-3} (for particles with diameters between 3 – 80 nm) for simulations similar to (a) MOD_noHetLossHPMTF and (b) MOD relative to simulations BASE, except all with no sea salt debromination. Simulations are described in Table 5.

525

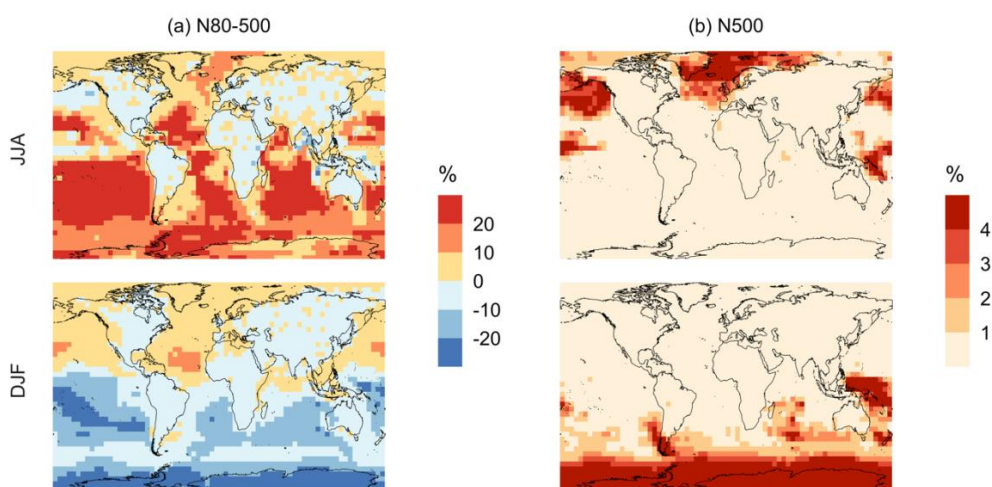


Figure A5 Geographic distribution of percent difference in seasonal-mean surface-layer aerosol number concentration in cm^{-3} for simulations similar to MOD_noHetLossHPMTF relative to simulations BASE, for particle diameters between (a) 80 – 500 nm and (b) > 500 nm. Simulations are described in Table 5.

526

527

528



529 **Data availability.** The DMS observational data in Fig. 6 were obtained from the referenced paper
530 (Kouvarakis and Mihalopoulos 2002). The observations data during ATom-4 are published
531 through the Distributed Active Archive Center for Biogeochemical Dynamics (DAAC) at (Novak
532 et al., 2021; Wollesen de Jonge et al., 2021) and <https://doi.org/10.3334/ORNLDAAC/1921>.

533 **Author contributions.** LT and WCP designed the research goals, aims, and methodology,
534 implemented the new code into GC-TOMAS. QC, BA, CHF and CDH contributed in code
535 development. All authors provided expert advice on data analysis, interpretation, and visualization.
536 LT ran model simulations, analyzed the data, created the figures, and led manuscript development
537 and editing.

538 **Competing interests.** The contact authors have declared that none of the authors has any
539 competing interests.

540 **Acknowledgements.** LT and WCP gratefully acknowledge Ka Ming Fung for discussions on
541 DMS oxidation chemistry. BC thanks Rachel Y.-W. Chang for discussions on marine aerosols.

542 **Financial support.** LT and WCP was supported by NSF grant no. 2155192. QC was supported
543 by the Hong Kong Research Grants Council (Grant No. 15223221 and 15219722). BA was
544 supported by NSF AGS 2109323 and PLR 1904128. CHF was supported by NASA FINESST
545 (grant 80NSSC19K1368). CDH acknowledges funding support from NSF AGS (grant 1848372).
546 BA gratefully acknowledges research funding supported by the Ocean Frontier Institute, through
547 an award from the Canada First Research Excellence Fund. JRP was supported by the Atmospheric
548 System Research (ASR) program, part of the US Department of Energy's Office of Biological and
549 Environmental Research within the Office of Science, under grant DE-SC0021208. SI was
550 supported by Ferring Pharmaceuticals through the Extreme Environments research Laboratory,
551 École Polytechnique Fédérale de Lausanne (EPFL).

552 References

553 Adams, P. J. and Seinfeld, J. H.: Predicting global aerosol size distributions in general circulation
554 models, *J. Geophys. Res. Atmospheres*, 107, AAC 4-1-AAC 4-23,
555 <https://doi.org/10.1029/2001JD001010>, 2002.

556 Alexander, B., Park, R. J., Jacob, D. J., Li, Q. B., Yantosca, R. M., Savarino, J., Lee, C. C. W., and
557 Thiemens, M. H.: Sulfate formation in sea-salt aerosols: Constraints from oxygen isotopes, *J.*
558 *Geophys. Res. Atmospheres*, 110, <https://doi.org/10.1029/2004JD005659>, 2005.

559 Amos, H. M., Jacob, D. J., Holmes, C. D., Fisher, J. A., Wang, Q., Yantosca, R. M., Corbitt, E. S.,
560 Galarneau, E., Rutter, A. P., Gustin, M. S., Steffen, A., Schauer, J. J., Graydon, J. A., Louis, V. L.
561 S., Talbot, R. W., Edgerton, E. S., Zhang, Y., and Sunderland, E. M.: Gas-particle partitioning of
562 atmospheric Hg(II) and its effect on global mercury deposition, *Atmospheric Chem. Phys.*, 12,
563 591–603, <https://doi.org/10.5194/acp-12-591-2012>, 2012.

564 Atkinson, R., Baulch, D. L., Cox, R. A., Crowley, J. N., Hampson, R. F., Hynes, R. G., Jenkin, M.
565 E., Rossi, M. J., and Troe, J.: Evaluated kinetic and photochemical data for atmospheric chemistry:
566 Volume I - gas phase reactions of O_x, HO_x, NO_x and SO_x species, *Atmospheric Chem. Phys.*, 4,
567 1461–1738, <https://doi.org/10.5194/acp-4-1461-2004>, 2004.



- 568 Bardouki, H., da Rosa, M. B., Mihalopoulos, N., Palm, W.-U., and Zetzsch, C.: Kinetics and
569 mechanism of the oxidation of dimethylsulfoxide (DMSO) and methanesulfinat (MSI⁻) by OH
570 radicals in aqueous medium, *Atmos. Environ.*, 36, 4627–4634, [https://doi.org/10.1016/S1352-](https://doi.org/10.1016/S1352-2310(02)00460-0)
571 2310(02)00460-0, 2002.
- 572 Barnes, I., Hjorth, J., and Mihalopoulos, N.: Dimethyl Sulfide and Dimethyl Sulfoxide and Their
573 Oxidation in the Atmosphere, *Chem. Rev.*, 106, 940–975, <https://doi.org/10.1021/cr020529+>,
574 2006.
- 575 Berndt, T., Scholz, W., Mentler, B., Fischer, L., Hoffmann, E. H., Tilgner, A., Hyttinen, N., Prisle,
576 N. L., Hansel, A., and Herrmann, H.: Fast Peroxy Radical Isomerization and OH Recycling in the
577 Reaction of OH Radicals with Dimethyl Sulfide, *J. Phys. Chem. Lett.*, 10, 6478–6483,
578 <https://doi.org/10.1021/acs.jpcllett.9b02567>, 2019.
- 579 Bey, I., Jacob, D. J., Yantosca, R. M., Logan, J. A., Field, B. D., Fiore, A. M., Li, Q., Liu, H. Y.,
580 Mickley, L. J., and Schultz, M. G.: Global modeling of tropospheric chemistry with assimilated
581 meteorology: Model description and evaluation, *J. Geophys. Res. Atmospheres*, 106, 23073–
582 23095, <https://doi.org/10.1029/2001JD000807>, 2001.
- 583 Boniface, J., Shi, Q., Li, Y. Q., Cheung, J. L., Rattigan, O. V., Davidovits, P., Worsnop, D. R.,
584 Jayne, J. T., and Kolb, C. E.: Uptake of Gas-Phase SO₂, H₂S, and CO₂ by Aqueous Solutions, *J.*
585 *Phys. Chem. A*, 104, 7502–7510, <https://doi.org/10.1021/jp000479h>, 2000.
- 586 Boucher, O., Moulin, C., Belviso, S., Aumont, O., Bopp, L., Cosme, E., von Kuhlmann, R.,
587 Lawrence, M. G., Pham, M., Reddy, M. S., Sciare, J., and Venkataraman, C.: DMS atmospheric
588 concentrations and sulphate aerosol indirect radiative forcing: a sensitivity study to the DMS
589 source representation and oxidation, *Atmospheric Chem. Phys.*, 3, 49–65,
590 <https://doi.org/10.5194/acp-3-49-2003>, 2003.
- 591 Breider, T. J., Chipperfield, M. P., Richards, N. a. D., Carslaw, K. S., Mann, G. W., and Spracklen,
592 D. V.: Impact of BrO on dimethylsulfide in the remote marine boundary layer, *Geophys. Res. Lett.*,
593 37, <https://doi.org/10.1029/2009GL040868>, 2010.
- 594 Burkholder, J. B., Sander, S. P., Abbatt, J. P. D., Barker, J. R., Huie, R. E., Kolb, C. E., Kurylo,
595 M. J., Orkin, V. L., Wilmouth, D. M., and Wine, P. H.: Chemical kinetics and photochemical data
596 for use in atmospheric studies: evaluation number 18, 2015.
- 597 Burkholder, J. B., Sander, S. P., Abbatt, J. P. D., Barker, J. R., Cappa, C., Crouse, J. D., Dibble,
598 T. S., Huie, R. E., Kolb, C. E., Kurylo, M. J., Orkin, V. L., Percival, C. J., Wilmouth, D. M., and
599 Wine, P. H.: Chemical kinetics and photochemical data for use in atmospheric studies; evaluation
600 number 19, 2020.
- 601 Carslaw, K. S., Lee, L. A., Reddington, C. L., Pringle, K. J., Rap, A., Forster, P. M., Mann, G. W.,
602 Spracklen, D. V., Woodhouse, M. T., Regayre, L. A., and Pierce, J. R.: Large contribution of
603 natural aerosols to uncertainty in indirect forcing, *Nature*, 503, 67–71,
604 <https://doi.org/10.1038/nature12674>, 2013.



- 605 Charlson, R. J., Lovelock, J. E., Andreae, M. O., and Warren, S. G.: Oceanic phytoplankton,
606 atmospheric sulphur, cloud albedo and climate, *Nature*, 326, 655–661,
607 <https://doi.org/10.1038/326655a0>, 1987.
- 608 Chen, H., Ezell, M. J., Arquero, K. D., Varner, M. E., Dawson, M. L., Gerber, R. B., and Finlayson-
609 Pitts, B. J.: New particle formation and growth from methanesulfonic acid, trimethylamine and
610 water, *Phys. Chem. Chem. Phys.*, 17, 13699–13709, <https://doi.org/10.1039/C5CP00838G>, 2015.
- 611 Chen, Q., Geng, L., Schmidt, J. A., Xie, Z., Kang, H., Dachs, J., Cole-Dai, J., Schauer, A. J., Camp,
612 M. G., and Alexander, B.: Isotopic constraints on the role of hypohalous acids in sulfate aerosol
613 formation in the remote marine boundary layer, *Atmospheric Chem. Phys.*, 16, 11433–11450,
614 <https://doi.org/10.5194/acp-16-11433-2016>, 2016.
- 615 Chen, Q., Schmidt, J. A., Shah, V., Jaeglé, L., Sherwen, T., and Alexander, B.: Sulfate production
616 by reactive bromine: Implications for the global sulfur and reactive bromine budgets, *Geophys.*
617 *Res. Lett.*, 44, 7069–7078, <https://doi.org/10.1002/2017GL073812>, 2017.
- 618 Chen, Q., Sherwen, T., Evans, M., and Alexander, B.: DMS oxidation and sulfur aerosol formation
619 in the marine troposphere: a focus on reactive halogen and multiphase chemistry, *Atmospheric*
620 *Chem. Phys.*, 18, 13617–13637, <https://doi.org/10.5194/acp-18-13617-2018>, 2018.
- 621 Chin, M., Jacob, D. J., Gardner, G. M., Foreman-Fowler, M. S., Spiro, P. A., and Savoie, D. L.: A
622 global three-dimensional model of tropospheric sulfate, *J. Geophys. Res. Atmospheres*, 101,
623 18667–18690, <https://doi.org/10.1029/96JD01221>, 1996.
- 624 Clarke, A. D., Davis, D., Kapustin, V. N., Eisele, F., Chen, G., Paluch, I., Lenschow, D., Bandy,
625 A. R., Thornton, D., Moore, K., Mauldin, L., Tanner, D., Litchy, M., Carroll, M. A., Collins, J.,
626 and Albercook, G.: Particle Nucleation in the Tropical Boundary Layer and Its Coupling to Marine
627 Sulfur Sources, *Science*, 282, 89–92, 1998a.
- 628 Clarke, A. D., Varner, J. L., Eisele, F., Mauldin, R. L., Tanner, D., and Litchy, M.: Particle
629 production in the remote marine atmosphere: Cloud outflow and subsidence during ACE 1, *J.*
630 *Geophys. Res. Atmospheres*, 103, 16397–16409, <https://doi.org/10.1029/97JD02987>, 1998b.
- 631 Du, L., Xu, Y., Ge, M., Jia, L., Yao, L., and Wang, W.: Rate constant of the gas phase reaction of
632 dimethyl sulfide (CH₃SCH₃) with ozone, *Chem. Phys. Lett.*, 436, 36–40,
633 <https://doi.org/10.1016/j.cplett.2007.01.025>, 2007.
- 634 Duncan Fairlie, T., Jacob, D. J., and Park, R. J.: The impact of transpacific transport of mineral
635 dust in the United States, *Atmos. Environ.*, 41, 1251–1266,
636 <https://doi.org/10.1016/j.atmosenv.2006.09.048>, 2007.
- 637 Emerson, E. W., Hodshire, A. L., DeBolt, H. M., Bilsback, K. R., Pierce, J. R., McMeeking, G.
638 R., and Farmer, D. K.: Revisiting particle dry deposition and its role in radiative effect estimates,
639 *Proc. Natl. Acad. Sci.*, 117, 26076–26082, <https://doi.org/10.1073/pnas.2014761117>, 2020.
- 640 Enami, S., Nakano, Y., Hashimoto, S., Kawasaki, M., Aloisio, S., and Francisco, J. S.: Reactions
641 of Cl Atoms with Dimethyl Sulfide: A Theoretical Calculation and an Experimental Study with



- 642 Cavity Ring-Down Spectroscopy, *J. Phys. Chem. A*, 108, 7785–7789,
643 <https://doi.org/10.1021/jp049772y>, 2004.
- 644 Falona, I.: Sulfur processing in the marine atmospheric boundary layer: A review and critical
645 assessment of modeling uncertainties, *Atmos. Environ.*, 43, 2841–2854,
646 <https://doi.org/10.1016/j.atmosenv.2009.02.043>, 2009.
- 647 Flyunt, R., Makogon, O., Schuchmann, M. N., Asmus, K.-D., and Sonntag, C. von: OH-Radical-
648 induced oxidation of methanesulfonic acid. The reactions of the methanesulfonyl radical in the
649 absence and presence of dioxygen, *J. Chem. Soc. Perkin Trans. 2*, 787–792,
650 <https://doi.org/10.1039/B009631H>, 2001.
- 651 Fung, K. M., Heald, C. L., Kroll, J. H., Wang, S., Jo, D. S., Gettelman, A., Lu, Z., Liu, X., Zaveri,
652 R. A., Apel, E. C., Blake, D. R., Jimenez, J.-L., Campuzano-Jost, P., Veres, P. R., Bates, T. S.,
653 Shilling, J. E., and Zawadowicz, M.: Exploring dimethyl sulfide (DMS) oxidation and implications
654 for global aerosol radiative forcing, *Atmospheric Chem. Phys.*, 22, 1549–1573,
655 <https://doi.org/10.5194/acp-22-1549-2022>, 2022.
- 656 Galí, M., Levasseur, M., Devred, E., Simó, R., and Babin, M.: Sea-surface dimethylsulfide (DMS)
657 concentration from satellite data at global and regional scales, *Biogeosciences*, 15, 3497–3519,
658 <https://doi.org/10.5194/bg-15-3497-2018>, 2018.
- 659 Galí, M., Devred, E., Babin, M., and Levasseur, M.: Decadal increase in Arctic dimethylsulfide
660 emission, *Proc. Natl. Acad. Sci.*, 116, 19311–19317, <https://doi.org/10.1073/pnas.1904378116>,
661 2019.
- 662 Gershenson, M., Davidovits, P., Jayne, J. T., Kolb, C. E., and Worsnop, D. R.: Simultaneous
663 Uptake of DMS and Ozone on Water, *J. Phys. Chem. A*, 105, 7031–7036,
664 <https://doi.org/10.1021/jp010696y>, 2001.
- 665 von Glasow, R. and Crutzen, P. J.: Model study of multiphase DMS oxidation with a focus on
666 halogens, *Atmospheric Chem. Phys.*, 4, 589–608, <https://doi.org/10.5194/acp-4-589-2004>, 2004.
- 667 Hodshire, A. L., Campuzano-Jost, P., Kodros, J. K., Croft, B., Nault, B. A., Schroder, J. C.,
668 Jimenez, J. L., and Pierce, J. R.: The potential role of methanesulfonic acid (MSA) in aerosol
669 formation and growth and the associated radiative forcings, *Atmospheric Chem. Phys.*, 19, 3137–
670 3160, <https://doi.org/10.5194/acp-19-3137-2019>, 2019.
- 671 Hoffmann, E. H., Tilgner, A., Schrödner, R., Bräuer, P., Wolke, R., and Herrmann, H.: An
672 advanced modeling study on the impacts and atmospheric implications of multiphase dimethyl
673 sulfide chemistry, *Proc. Natl. Acad. Sci.*, 113, 11776–11781,
674 <https://doi.org/10.1073/pnas.1606320113>, 2016.
- 675 Hoffmann, E. H., Heinold, B., Kubin, A., Tegen, I., and Herrmann, H.: The Importance of the
676 Representation of DMS Oxidation in Global Chemistry-Climate Simulations, *Geophys. Res. Lett.*,
677 48, e2021GL094068, <https://doi.org/10.1029/2021GL094068>, 2021.



- 678 Holmes, C. D., Bertram, T. H., Confer, K. L., Graham, K. A., Ronan, A. C., Wirks, C. K., and
679 Shah, V.: The Role of Clouds in the Tropospheric NO_x Cycle: A New Modeling Approach for
680 Cloud Chemistry and Its Global Implications, *Geophys. Res. Lett.*, 46, 4980–4990,
681 <https://doi.org/10.1029/2019GL081990>, 2019.
- 682 Hoyle, C. R., Fuchs, C., Järvinen, E., Saathoff, H., Dias, A., El Haddad, I., Gysel, M., Coburn, S.
683 C., Tröstl, J., Bernhammer, A.-K., Bianchi, F., Breitenlechner, M., Corbin, J. C., Craven, J.,
684 Donahue, N. M., Duplissy, J., Ehrhart, S., Frege, C., Gordon, H., Höppel, N., Heinritzi, M.,
685 Kristensen, T. B., Molteni, U., Nichman, L., Pinterich, T., Prévôt, A. S. H., Simon, M., Slowik, J.
686 G., Steiner, G., Tomé, A., Vogel, A. L., Volkamer, R., Wagner, A. C., Wagner, R., Wexler, A. S.,
687 Williamson, C., Winkler, P. M., Yan, C., Amorim, A., Dommen, J., Curtius, J., Gallagher, M. W.,
688 Flagan, R. C., Hansel, A., Kirkby, J., Kulmala, M., Möhler, O., Stratmann, F., Worsnop, D. R.,
689 and Baltensperger, U.: Aqueous phase oxidation of sulphur dioxide by ozone in cloud droplets,
690 *Atmospheric Chem. Phys.*, 16, 1693–1712, <https://doi.org/10.5194/acp-16-1693-2016>, 2016.
- 691 Ishino, S., Hattori, S., Legrand, M., Chen, Q., Alexander, B., Shao, J., Huang, J., Jaeglé, L.,
692 Jourdain, B., Preunkert, S., Yamada, A., Yoshida, N., and Savarino, J.: Regional Characteristics
693 of Atmospheric Sulfate Formation in East Antarctica Imprinted on 17O-Excess Signature, *J.*
694 *Geophys. Res. Atmospheres*, 126, e2020JD033583, <https://doi.org/10.1029/2020JD033583>, 2021.
- 695 Jacob, D. J., Field, B. D., Li, Q., Blake, D. R., de Gouw, J., Warneke, C., Hansel, A., Wisthaler,
696 A., Singh, H. B., and Guenther, A.: Global budget of methanol: Constraints from atmospheric
697 observations, *J. Geophys. Res. Atmospheres*, 110, <https://doi.org/10.1029/2004JD005172>, 2005.
- 698 Jernigan, C. M., Fite, C. H., Vereecken, L., Berkelhammer, M. B., Rollins, A. W., Rickly, P. S.,
699 Novelli, A., Taraborrelli, D., Holmes, C. D., and Bertram, T. H.: Efficient Production of Carbonyl
700 Sulfide in the Low-NO_x Oxidation of Dimethyl Sulfide, *Geophys. Res. Lett.*, 49, e2021GL096838,
701 <https://doi.org/10.1029/2021GL096838>, 2022a.
- 702 Jernigan, C. M., Cappa, C. D., and Bertram, T. H.: Reactive Uptake of Hydroperoxymethyl
703 Thioformate to Sodium Chloride and Sodium Iodide Aerosol Particles, *J. Phys. Chem. A*, 126,
704 4476–4481, <https://doi.org/10.1021/acs.jpca.2c03222>, 2022b.
- 705 Johnson, J. S. and Jen, C. N.: Role of Methanesulfonic Acid in Sulfuric Acid–Amine and Ammonia
706 New Particle Formation, *ACS Earth Space Chem.*, 7, 653–660,
707 <https://doi.org/10.1021/acsearthspacechem.3c00017>, 2023.
- 708 Johnson, M. T.: A numerical scheme to calculate temperature and salinity dependent air-water
709 transfer velocities for any gas, *Ocean Sci.*, 6, 913–932, <https://doi.org/10.5194/os-6-913-2010>,
710 2010.
- 711 Kaufman, Y. J. and Tanré, D.: Effect of variations in super-saturation on the formation of cloud
712 condensation nuclei, *Nature*, 369, 45–48, <https://doi.org/10.1038/369045a0>, 1994.
- 713 Khan, M. A. H., Gillespie, S. M. P., Razis, B., Xiao, P., Davies-Coleman, M. T., Percival, C. J.,
714 Derwent, R. G., Dyke, J. M., Ghosh, M. V., Lee, E. P. F., and Shallcross, D. E.: A modelling study
715 of the atmospheric chemistry of DMS using the global model, STOCHEM-CRI, *Atmos. Environ.*,
716 127, 69–79, <https://doi.org/10.1016/j.atmosenv.2015.12.028>, 2016.



- 717 Kloster, S., Feichter, J., Maier-Reimer, E., Six, K. D., Stier, P., and Wetzel, P.: DMS cycle in the
718 marine ocean-atmosphere system – a global model study, *Biogeosciences*, 3, 29–51,
719 <https://doi.org/10.5194/bg-3-29-2006>, 2006.
- 720 Kodros, J. K. and Pierce, J. R.: Important global and regional differences in aerosol cloud-albedo
721 effect estimates between simulations with and without prognostic aerosol microphysics, *J.*
722 *Geophys. Res. Atmospheres*, 122, 4003–4018, <https://doi.org/10.1002/2016JD025886>, 2017.
- 723 Kodros, J. K., Cucinotta, R., Ridley, D. A., Wiedinmyer, C., and Pierce, J. R.: The aerosol radiative
724 effects of uncontrolled combustion of domestic waste, *Atmospheric Chem. Phys.*, 16, 6771–6784,
725 <https://doi.org/10.5194/acp-16-6771-2016>, 2016.
- 726 Kouvarakis, G. and Mihalopoulos, N.: Seasonal variation of dimethylsulfide in the gas phase and
727 of methanesulfonate and non-sea-salt sulfate in the aerosols phase in the Eastern Mediterranean
728 atmosphere, *Atmos. Environ.*, 36, 929–938, [https://doi.org/10.1016/S1352-2310\(01\)00511-8](https://doi.org/10.1016/S1352-2310(01)00511-8),
729 2002.
- 730 Kowalczyk, P., Cooper, W. J., Whitehead, R. F., Durako, M. J., and Sheldon, W.: Characterization
731 of CDOM in an organic-rich river and surrounding coastal ocean in the South Atlantic Bight,
732 *Aquat. Sci.*, 65, 384–401, <https://doi.org/10.1007/s00027-003-0678-1>, 2003.
- 733 Kulmala, M.: How Particles Nucleate and Grow, *Science*, 302, 1000–1001,
734 <https://doi.org/10.1126/science.1090848>, 2003.
- 735 Kulmala, M., Pirjola, L., and Mäkelä, J. M.: Stable sulphate clusters as a source of new
736 atmospheric particles, *Nature*, 404, 66–69, <https://doi.org/10.1038/35003550>, 2000.
- 737 Lana, A., Bell, T. G., Simó, R., Vallina, S. M., Ballabrera-Poy, J., Kettle, A. J., Dachs, J., Bopp,
738 L., Saltzman, E. S., Stefels, J., Johnson, J. E., and Liss, P. S.: An updated climatology of surface
739 dimethylsulfide concentrations and emission fluxes in the global ocean, *Glob. Biogeochem.*
740 *Cycles*, 25, <https://doi.org/10.1029/2010GB003850>, 2011.
- 741 Leaitch, W. R., Sharma, S., Huang, L., Toom-Saunty, D., Chivulescu, A., Macdonald, A. M., von
742 Salzen, K., Pierce, J. R., Bertram, A. K., Schroder, J. C., Shantz, N. C., Chang, R. Y.-W., and
743 Norman, A.-L.: Dimethyl sulfide control of the clean summertime Arctic aerosol and cloud, *Elem.*
744 *Sci. Anthr.*, 1, 000017, <https://doi.org/10.12952/journal.elementa.000017>, 2013.
- 745 Lee, Y. H. and Adams, P. J.: A Fast and Efficient Version of the TwO-Moment Aerosol Sectional
746 (TOMAS) Global Aerosol Microphysics Model, *Aerosol Sci. Technol.*, 46, 678–689,
747 <https://doi.org/10.1080/02786826.2011.643259>, 2012.
- 748 Lee, Y. H., Pierce, J. R., and Adams, P. J.: Representation of nucleation mode microphysics in a
749 global aerosol model with sectional microphysics, *Geosci. Model Dev.*, 6, 1221–1232,
750 <https://doi.org/10.5194/gmd-6-1221-2013>, 2013.
- 751 Liu, H., Jacob, D. J., Bey, I., and Yantosca, R. M.: Constraints from ²¹⁰Pb and ⁷Be on wet
752 deposition and transport in a global three-dimensional chemical tracer model driven by assimilated



- 753 meteorological fields, *J. Geophys. Res. Atmospheres*, 106, 12109–12128,
754 <https://doi.org/10.1029/2000JD900839>, 2001.
- 755 Lucas, D. D. and Prinn, R. G.: Mechanistic studies of dimethylsulfide oxidation products using an
756 observationally constrained model, *J. Geophys. Res. Atmospheres*, 107, ACH 12-1-ACH 12-26,
757 <https://doi.org/10.1029/2001JD000843>, 2002.
- 758 Napari, I., Noppel, M., Vehkamäki, H., and Kulmala, M.: Parametrization of ternary nucleation
759 rates for H₂SO₄-NH₃-H₂O vapors, *J. Geophys. Res. Atmospheres*, 107, AAC 6-1-AAC 6-6,
760 <https://doi.org/10.1029/2002JD002132>, 2002.
- 761 Nightingale, P. D., Malin, G., Law, C. S., Watson, A. J., Liss, P. S., Liddicoat, M. I., Boutin, J.,
762 and Upstill-Goddard, R. C.: In situ evaluation of air-sea gas exchange parameterizations using
763 novel conservative and volatile tracers, *Glob. Biogeochem. Cycles*, 14, 373–387,
764 <https://doi.org/10.1029/1999GB900091>, 2000.
- 765 Novak, G. A., Fite, C. H., Holmes, C. D., Veres, P. R., Neuman, J. A., Faloona, I., Thornton, J. A.,
766 Wolfe, G. M., Vermeuel, M. P., Jernigan, C. M., Peischl, J., Ryerson, T. B., Thompson, C. R.,
767 Bourgeois, I., Warneke, C., Gkatzelis, G. I., Coggon, M. M., Sekimoto, K., Bui, T. P., Dean-Day,
768 J., Diskin, G. S., DiGangi, J. P., Nowak, J. B., Moore, R. H., Wiggins, E. B., Winstead, E. L.,
769 Robinson, C., Thornhill, K. L., Sanchez, K. J., Hall, S. R., Ullmann, K., Dollner, M., Weinzierl,
770 B., Blake, D. R., and Bertram, T. H.: Rapid cloud removal of dimethyl sulfide oxidation products
771 limits SO₂ and cloud condensation nuclei production in the marine atmosphere, *Proc. Natl. Acad. Sci.*,
772 118, e2110472118, <https://doi.org/10.1073/pnas.2110472118>, 2021.
- 773 Novak, G. A., Kilgour, D. B., Jernigan, C. M., Vermeuel, M. P., and Bertram, T. H.: Oceanic
774 emissions of dimethyl sulfide and methanethiol and their contribution to sulfur dioxide production
775 in the marine atmosphere, *Atmospheric Chem. Phys.*, 22, 6309–6325, <https://doi.org/10.5194/acp-22-6309-2022>, 2022.
- 777 Park, R. J., Jacob, D. J., Field, B. D., Yantosca, R. M., and Chin, M.: Natural and transboundary
778 pollution influences on sulfate-nitrate-ammonium aerosols in the United States: Implications for
779 policy, *J. Geophys. Res. Atmospheres*, 109, <https://doi.org/10.1029/2003JD004473>, 2004.
- 780 Parrella, J. P., Jacob, D. J., Liang, Q., Zhang, Y., Mickle, L. J., Miller, B., Evans, M. J., Yang,
781 X., Pyle, J. A., Theys, N., and Van Roozendaal, M.: Tropospheric bromine chemistry: implications
782 for present and pre-industrial ozone and mercury, *Atmospheric Chem. Phys.*, 12, 6723–6740,
783 <https://doi.org/10.5194/acp-12-6723-2012>, 2012.
- 784 Patroescu, I. V., Barnes, I., and Becker, K. H.: FTIR Kinetic and Mechanistic Study of the
785 Atmospheric Chemistry of Methyl Thiolfornate, *J. Phys. Chem.*, 100, 17207–17217,
786 <https://doi.org/10.1021/jp961452u>, 1996.
- 787 Pham, M., Müller, J.-F., Brasseur, G. P., Granier, C., and Mégie, G.: A three-dimensional study of
788 the tropospheric sulfur cycle, *J. Geophys. Res. Atmospheres*, 100, 26061–26092,
789 <https://doi.org/10.1029/95JD02095>, 1995.



- 790 Pierce, J. R. and Adams, P. J.: Global evaluation of CCN formation by direct emission of sea salt
791 and growth of ultrafine sea salt, *J. Geophys. Res. Atmospheres*, 111,
792 <https://doi.org/10.1029/2005JD006186>, 2006.
- 793 Pound, R. J., Sherwen, T., Helmig, D., Carpenter, L. J., and Evans, M. J.: Influences of oceanic
794 ozone deposition on tropospheric photochemistry, *Atmospheric Chem. Phys.*, 20, 4227–4239,
795 <https://doi.org/10.5194/acp-20-4227-2020>, 2020.
- 796 Pye, H. O. T., Liao, H., Wu, S., Mickley, L. J., Jacob, D. J., Henze, D. K., and Seinfeld, J. H.:
797 Effect of changes in climate and emissions on future sulfate-nitrate-ammonium aerosol levels in
798 the United States, *J. Geophys. Res. Atmospheres*, 114, <https://doi.org/10.1029/2008JD010701>,
799 2009.
- 800 Rosati, B., Isokääntä, S., Christiansen, S., Jensen, M. M., Moosakutty, S. P., Wollesen de Jonge,
801 R., Massling, A., Glasius, M., Elm, J., Virtanen, A., and Bilde, M.: Hygroscopicity and CCN
802 potential of DMS-derived aerosol particles, *Atmospheric Chem. Phys.*, 22, 13449–13466,
803 <https://doi.org/10.5194/acp-22-13449-2022>, 2022.
- 804 Saunders, S. M., Jenkin, M. E., Derwent, R. G., and Pilling, M. J.: Protocol for the development
805 of the Master Chemical Mechanism, MCM v3 (Part A): tropospheric degradation of non-aromatic
806 volatile organic compounds, *Atmospheric Chem. Phys.*, 3, 161–180, <https://doi.org/10.5194/acp-3-161-2003>, 2003.
- 808 Schmidt, J. A., Jacob, D. J., Horowitz, H. M., Hu, L., Sherwen, T., Evans, M. J., Liang, Q.,
809 Suleiman, R. M., Oram, D. E., Le Breton, M., Percival, C. J., Wang, S., Dix, B., and Volkamer,
810 R.: Modeling the observed tropospheric BrO background: Importance of multiphase chemistry and
811 implications for ozone, OH, and mercury, *J. Geophys. Res. Atmospheres*, 121, 11,819–11,835,
812 <https://doi.org/10.1002/2015JD024229>, 2016.
- 813 Schobesberger, S., Junninen, H., Bianchi, F., Lönn, G., Ehn, M., Lehtipalo, K., Dommen, J.,
814 Ehrhart, S., Ortega, I. K., Franchin, A., Nieminen, T., Riccobono, F., Hutterli, M., Duplissy, J.,
815 Almeida, J., Amorim, A., Breitenlechner, M., Downard, A. J., Dunne, E. M., Flagan, R. C., Kajos,
816 M., Keskinen, H., Kirkby, J., Kupc, A., Kürten, A., Kurtén, T., Laaksonen, A., Mathot, S., Onnela,
817 A., Praplan, A. P., Rondo, L., Santos, F. D., Schallhart, S., Schnitzhofer, R., Sipilä, M., Tomé, A.,
818 Tsagkogeorgas, G., Vehkamäki, H., Wimmer, D., Baltensperger, U., Carslaw, K. S., Curtius, J.,
819 Hansel, A., Petäjä, T., Kulmala, M., Donahue, N. M., and Worsnop, D. R.: Molecular
820 understanding of atmospheric particle formation from sulfuric acid and large oxidized organic
821 molecules, *Proc. Natl. Acad. Sci.*, 110, 17223–17228, <https://doi.org/10.1073/pnas.1306973110>,
822 2013.
- 823 Sehested, K. and Holcman, J.: A pulse radiolysis study of the OH radical induced autoxidation of
824 methanesulfinic acid, *Radiat. Phys. Chem.*, 47, 357–360, [https://doi.org/10.1016/0969-806X\(95\)00115-E](https://doi.org/10.1016/0969-806X(95)00115-E), 1996.
- 826 Sherwen, T., Schmidt, J. A., Evans, M. J., Carpenter, L. J., Großmann, K., Eastham, S. D., Jacob,
827 D. J., Dix, B., Koenig, T. K., Sinreich, R., Ortega, I., Volkamer, R., Saiz-Lopez, A., Prados-
828 Roman, C., Mahajan, A. S., and Ordóñez, C.: Global impacts of tropospheric halogens (Cl, Br, I)



- 829 on oxidants and composition in GEOS-Chem, *Atmospheric Chem. Phys.*, 16, 12239–12271,
830 <https://doi.org/10.5194/acp-16-12239-2016>, 2016a.
- 831 Sherwen, T. M., Evans, M. J., Spracklen, D. V., Carpenter, L. J., Chance, R., Baker, A. R.,
832 Schmidt, J. A., and Breider, T. J.: Global modeling of tropospheric iodine aerosol, *Geophys. Res.*
833 *Lett.*, 43, 10012–10019, <https://doi.org/10.1002/2016GL070062>, 2016b.
- 834 Sipilä, M., Berndt, T., Petäjä, T., Brus, D., Vanhanen, J., Stratmann, F., Patokoski, J., Mauldin, R.
835 L., Hyvärinen, A.-P., Lihavainen, H., and Kulmala, M.: The Role of Sulfuric Acid in Atmospheric
836 Nucleation, *Science*, 327, 1243–1246, <https://doi.org/10.1126/science.1180315>, 2010.
- 837 Spracklen, D. V., Pringle, K. J., Carslaw, K. S., Chipperfield, M. P., and Mann, G. W.: A global
838 off-line model of size-resolved aerosol microphysics: I. Model development and prediction of
839 aerosol properties, *Atmospheric Chem. Phys.*, 5, 2227–2252, [https://doi.org/10.5194/acp-5-2227-](https://doi.org/10.5194/acp-5-2227-2005)
840 2005, 2005.
- 841 Thomas, M. A., Suntharalingam, P., Pozzoli, L., Rast, S., Devasthale, A., Kloster, S., Feichter, J.,
842 and Lenton, T. M.: Quantification of DMS aerosol-cloud-climate interactions using the ECHAM5-
843 HAMMOZ model in a current climate scenario, *Atmospheric Chem. Phys.*, 10, 7425–7438,
844 <https://doi.org/10.5194/acp-10-7425-2010>, 2010.
- 845 Trivitayanurak, W., Adams, P. J., Spracklen, D. V., and Carslaw, K. S.: Tropospheric aerosol
846 microphysics simulation with assimilated meteorology: model description and intermodel
847 comparison, *Atmospheric Chem. Phys.*, 8, 3149–3168, <https://doi.org/10.5194/acp-8-3149-2008>,
848 2008.
- 849 Vehkamäki, H., Kulmala, M., Napari, I., Lehtinen, K. E. J., Timmreck, C., Noppel, M., and
850 Laaksonen, A.: An improved parameterization for sulfuric acid–water nucleation rates for
851 tropospheric and stratospheric conditions, *J. Geophys. Res. Atmospheres*, 107, AAC 3-1-AAC 3-
852 10, <https://doi.org/10.1029/2002JD002184>, 2002.
- 853 Veres, P. R., Neuman, J. A., Bertram, T. H., Assaf, E., Wolfe, G. M., Williamson, C. J., Weinzierl,
854 B., Tilmes, S., Thompson, C. R., Thames, A. B., Schroder, J. C., Saiz-Lopez, A., Rollins, A. W.,
855 Roberts, J. M., Price, D., Peischl, J., Nault, B. A., Møller, K. H., Miller, D. O., Meinardi, S., Li,
856 Q., Lamarque, J.-F., Kupc, A., Kjaergaard, H. G., Kinnison, D., Jimenez, J. L., Jernigan, C. M.,
857 Hornbrook, R. S., Hills, A., Dollner, M., Day, D. A., Cuevas, C. A., Campuzano-Jost, P.,
858 Burkholder, J., Bui, T. P., Brune, W. H., Brown, S. S., Brock, C. A., Bourgeois, I., Blake, D. R.,
859 Apel, E. C., and Ryerson, T. B.: Global airborne sampling reveals a previously unobserved
860 dimethyl sulfide oxidation mechanism in the marine atmosphere, *Proc. Natl. Acad. Sci.*, 117,
861 4505–4510, <https://doi.org/10.1073/pnas.1919344117>, 2020.
- 862 Vermeuel, M. P., Novak, G. A., Jernigan, C. M., and Bertram, T. H.: Diel Profile of
863 Hydroperoxymethyl Thioformate: Evidence for Surface Deposition and Multiphase Chemistry,
864 *Environ. Sci. Technol.*, 54, 12521–12529, <https://doi.org/10.1021/acs.est.0c04323>, 2020.
- 865 Wang, W.-L., Song, G., Primeau, F., Saltzman, E. S., Bell, T. G., and Moore, J. K.: Global ocean
866 dimethyl sulfide climatology estimated from observations and an artificial neural network,
867 *Biogeosciences*, 17, 5335–5354, <https://doi.org/10.5194/bg-17-5335-2020>, 2020.



- 868 Wang, X., Jacob, D. J., Eastham, S. D., Sulprizio, M. P., Zhu, L., Chen, Q., Alexander, B.,
869 Sherwen, T., Evans, M. J., Lee, B. H., Haskins, J. D., Lopez-Hilfiker, F. D., Thornton, J. A., Huey,
870 G. L., and Liao, H.: The role of chlorine in global tropospheric chemistry, *Atmospheric Chem.*
871 *Phys.*, 19, 3981–4003, <https://doi.org/10.5194/acp-19-3981-2019>, 2019.
- 872 Wang, X., Jacob, D. J., Downs, W., Zhai, S., Zhu, L., Shah, V., Holmes, C. D., Sherwen, T.,
873 Alexander, B., Evans, M. J., Eastham, S. D., Neuman, J. A., Veres, P. R., Koenig, T. K., Volkamer,
874 R., Huey, L. G., Bannan, T. J., Percival, C. J., Lee, B. H., and Thornton, J. A.: Global tropospheric
875 halogen (Cl, Br, I) chemistry and its impact on oxidants, *Atmospheric Chem. Phys.*, 21, 13973–
876 13996, <https://doi.org/10.5194/acp-21-13973-2021>, 2021.
- 877 Wang, Y., Jacob, D. J., and Logan, J. A.: Global simulation of tropospheric O₃-NO_x-hydrocarbon
878 chemistry: 1. Model formulation, *J. Geophys. Res. Atmospheres*, 103, 10713–10725,
879 <https://doi.org/10.1029/98JD00158>, 1998.
- 880 Wesely, M. L.: Parameterization of surface resistances to gaseous dry deposition in regional-scale
881 numerical models, *Atmospheric Environ.* 1967, 23, 1293–1304, [https://doi.org/10.1016/0004-](https://doi.org/10.1016/0004-882)
882 [6981\(89\)90153-4](https://doi.org/10.1016/0004-6981(89)90153-4), 1989.
- 883 Westervelt, D. M., Pierce, J. R., Riipinen, I., Trivitayanurak, W., Hamed, A., Kulmala, M.,
884 Laaksonen, A., Decesari, S., and Adams, P. J.: Formation and growth of nucleated particles into
885 cloud condensation nuclei: model–measurement comparison, *Atmospheric Chem. Phys.*, 13,
886 7645–7663, <https://doi.org/10.5194/acp-13-7645-2013>, 2013.
- 887 Williamson, C. J., Kupc, A., Axisa, D., Bilsback, K. R., Bui, T., Campuzano-Jost, P., Dollner, M.,
888 Froyd, K. D., Hodshire, A. L., Jimenez, J. L., Kodros, J. K., Luo, G., Murphy, D. M., Nault, B. A.,
889 Ray, E. A., Weinzierl, B., Wilson, J. C., Yu, F., Yu, P., Pierce, J. R., and Brock, C. A.: A large
890 source of cloud condensation nuclei from new particle formation in the tropics, *Nature*, 574, 399–
891 403, <https://doi.org/10.1038/s41586-019-1638-9>, 2019.
- 892 Wollesen de Jonge, R., Elm, J., Rosati, B., Christiansen, S., Hyttinen, N., Lüdemann, D., Bilde,
893 M., and Roldin, P.: Secondary aerosol formation from dimethyl sulfide – improved mechanistic
894 understanding based on smog chamber experiments and modelling, *Atmospheric Chem. Phys.*, 21,
895 9955–9976, <https://doi.org/10.5194/acp-21-9955-2021>, 2021.
- 896 Wu, R., Wang, S., and Wang, L.: New Mechanism for the Atmospheric Oxidation of Dimethyl
897 Sulfide. The Importance of Intramolecular Hydrogen Shift in a CH₃SCH₂OO Radical, *J. Phys.*
898 *Chem. A*, 119, 112–117, <https://doi.org/10.1021/jp511616j>, 2015.
- 899 Zhang, J.-Z. and Millero, F. J.: The products from the oxidation of H₂S in seawater, *Geochim.*
900 *Cosmochim. Acta*, 57, 1705–1718, [https://doi.org/10.1016/0016-7037\(93\)90108-9](https://doi.org/10.1016/0016-7037(93)90108-9), 1993.
- 901 Zhang, Y., Jacob, D. J., Maasackers, J. D., Sulprizio, M. P., Sheng, J.-X., Gautam, R., and Worden,
902 J.: Monitoring global tropospheric OH concentrations using satellite observations of atmospheric
903 methane, *Atmospheric Chem. Phys.*, 18, 15959–15973, [https://doi.org/10.5194/acp-18-15959-](https://doi.org/10.5194/acp-18-15959-904)
904 [2018](https://doi.org/10.5194/acp-18-15959-2018), 2018.



- 905 Zhou, Z.-X., Lujan, S. A., Burkholder, A. B., Garbacz, M. A., and Kunkel, T. A.: Roles for DNA
906 polymerase δ in initiating and terminating leading strand DNA replication, *Nat. Commun.*, 10,
907 3992, <https://doi.org/10.1038/s41467-019-11995-z>, 2019.
- 908 Zhu, L., Nicovich, J. M., and Wine, P. H.: Temperature-dependent kinetics studies of aqueous
909 phase reactions of hydroxyl radicals with dimethylsulfoxide, dimethylsulfone, and
910 methanesulfonate, *Aquat. Sci.*, 65, 425–435, <https://doi.org/10.1007/s00027-003-0673-6>, 2003.
- 911 Zhu, L., Nenes, A., Wine, P. H., and Nicovich, J. M.: Effects of aqueous organosulfur chemistry
912 on particulate methanesulfonate to non-sea salt sulfate ratios in the marine atmosphere, *J.*
913 *Geophys. Res. Atmospheres*, 111, <https://doi.org/10.1029/2005JD006326>, 2006.
- 914 Zhu, L., Jacob, D. J., Eastham, S. D., Sulprizio, M. P., Wang, X., Sherwen, T., Evans, M. J., Chen,
915 Q., Alexander, B., Koenig, T. K., Volkamer, R., Huey, L. G., Le Breton, M., Bannan, T. J., and
916 Percival, C. J.: Effect of sea salt aerosol on tropospheric bromine chemistry, *Atmospheric Chem.*
917 *Phys.*, 19, 6497–6507, <https://doi.org/10.5194/acp-19-6497-2019>, 2019.

918